remote sensing

MDPI

Article

Co-Variability between the Surface Wind Divergence and Vorticity over the Ocean

Robert Jacobs * and Larry W. O'Neill

College of Earth, Ocean, and Atmospheric Sciences, Oregon State University, Corvallis, OR 97331, USA
* Correspondence: jacobrob@oregonstate.edu

Abstract: We examine the co-variability between the surface wind divergence and vorticity and how it varies with latitude in the Pacific Ocean using surface vector winds from reanalysis and satellite scatterometer observations. We show a strong correlation between divergence and vorticity throughout the extratropical oceans. From this observation, we develop a dynamical model to explain the first-order dynamics which govern this strong co-variability. Our model exploits the fact that for much of the time, the large-scale surface winds are approximately in a steady-state Ekman balance to first order. An angle α' is derived from Ekman dynamics by utilizing only the surface divergence and vorticity and is shown to succinctly summarize the co-variability between divergence and vorticity. This approach yields insight into the dynamics that shape the spatial variations in the large-scale surface wind field over the ocean; previous research has focused mainly on explaining variability in the vector winds rather than the derivative wind fields. Our model predicts two steady-state conditions which are easily identifiable as discrete peaks in α' Probability Distribution Functions (PDFs). In the Northern Hemisphere, steady-state conditions can be either (1) diverging, with negative vorticity, or (2) converging, with positive vorticity. We show that these two states correspond to relative high and low sea-level pressure features, respectively. Southern Hemisphere conditions are similar to those of the Northern Hemisphere, except with the opposite sign of vorticity. This model also predicts the latitudinal variations in the co-variability between divergence and vorticity due to the latitudinal variation in the Coriolis parameter. The main conclusion of this study is that the statistical co-variability between the surface divergence and vorticity over the ocean is consistent with Ekman dynamics and provides perhaps the first dynamical approach for interpreting their statistical distributions. The related α' PDFs provide a unique method for analyzing air–sea interactions and will likely have applications in evaluating the surface wind fields from scatterometers and weather and reanalysis models.

Keywords: divergence; vorticity; Ekman dynamics; ocean vector winds; QuikSCAT; ASCAT; ERA5

Citation: Jacobs, R.; O'Neill, L.W. Co-Variability between the Surface Wind Divergence and Vorticity over the Ocean. *Remote Sens.* **2024**, *16*, 451. https://doi.org/10.3390/rs16030451

Academic Editor: Gad Levy

Received: 22 November 2023
Revised: 9 January 2024
Accepted: 11 January 2024
Published: 24 January 2024

1. Introduction

Ocean surface wind vector measurements provide critical information for weather forecasting, climate study, ship route planning, and military operations [1]. These measurements are collected primarily through satellite remote sensing of the vector winds over the ocean using a constellation of satellite scatterometers. Scatterometers measure the ocean surface roughness which is directly linked to the surface wind speed and direction. This link is unique to the processing of each satellite scatterometer. Therefore, generating an intercalibrated ocean wind climate data record from multiple satellites that includes a research-quality dataset for the divergence and vorticity is imperative since these measures are sensitive indicators of subtle but important spatial variability in the surface wind field [2–5].

The surface divergence and vorticity, calculated from the wind field, are directly linked to vertical motion in the atmosphere and ocean [6–8] (i.e., precipitation and Ekman

pumping) and are important quantities in weather forecasting and research. Explaining variability in the divergence and vorticity thus provides important insight into the three-dimensional large-scale circulation of the atmosphere and upper ocean. However, a significant challenge exists in evaluating the accuracy of the scatterometer divergence and vorticity fields since there are practically no other independent means of estimating these fields from observational sources, although estimates are available from numerical weather prediction (NWP) reanalysis fields.

One key advantage of satellite surface vector wind measurements is the ability to estimate the spatial derivative wind fields, namely the divergence and vorticity, from simultaneous wind measurements over a large swath. Spatial wind derivatives contain two key and independent pieces of information beyond the wind vectors themselves: the spatial change in wind speed and direction, and a length scale over which the winds vary. Both pieces of information are driven by the underlying dynamics of the wind field and are limited by the accuracy of the winds and the spatial resolution capabilities of the satellite or model wind field from which they are derived. Point measurements such as buoy-mounted anemometers lack the spatial coverage by which to estimate spatial wind gradients, except in exceptionally rare cases in which an array of instruments is constructed. Scatterometers thus provide unique observations of key physical variables. The lack of independent derivative wind field measurements presents a challenge to evaluate the quality of the derivative wind fields from satellites. While challenging, progress has been made to quantify uncertainties in the spatial wind field derivatives [5,8–10]. Additionally, the dynamics that govern variability in the derivative wind fields in space and time and their associated statistical distributions have received relatively little research attention. One goal of this analysis is to develop an analytical metric to aid in evaluating statistical distributions of divergence and vorticity in the context of the leading-order dynamics governing the surface wind field. Besides improving our understanding of surface wind dynamics, this goal will partially address a key knowledge gap associated with how to independently evaluate scatterometer divergence and vorticity fields.

This research focuses on two satellite scatterometers, QuikSCAT and ASCAT-A, each of which provide long data records of accurate vector winds over most of the ice-free ocean. QuikSCAT was operational between October 1999 and November 2009, and ASCAT-A began operations in March 2007 and ended operations on 15 November 2021. Each instrument utilized an active microwave radar which infers surface winds by measuring the intensity of microwave radiation backscattered off the wind-roughened ocean surface from multiple viewing geometries. Different scatterometer products have different spatial resolution and wind vector qualities [1,11]. Moreover, Ku-band scatterometers, such as QuikSCAT, can suffer wind accuracy degradation from rain contamination in areas such as those with moist convection [12,13] and extratropical cyclones. Therefore, understanding the differences between scatterometer data and NWP models allows for the improvement of underrepresented processes in the models. For example, excessive mean zonal wind speed and low mean meridional wind speeds in model data (ERA5) compared with scatterometer observations result in excessive surface wind stress curl and has been theorized to be due to the absence of surface drag in the model data [14,15].

The analysis presented here focuses on interpreting the statistical co-variability of surface divergence and vorticity from instantaneous wind fields (Figure 1a–c). Most often, studies of satellite derivative wind fields focus on monthly or longer time averages of some process or phenomena [1,4,10,11,14–24] rather than the analysis of instantaneous fields [12,13,25–29]. Holbach and Bourassa [26] studied the vorticity variability of QuikSCAT vorticity fields in the eastern tropical Pacific to understand the effects of gap wind events on tropical cyclogenesis. The present study builds upon the previous research by analyzing the statistical distributions and physical processes associated with variability of the derivative wind fields. This analysis is made possible by the collection of long-duration and high-quality ocean vector wind data records [29]. This study also explains the leading-order statistical properties of the derivative wind fields in terms of the dynamics of large-scale

surface winds over the ocean. The improved understanding of the dynamics helps to highlight and explain the differences in spatial wind derivative fields between observations and models.

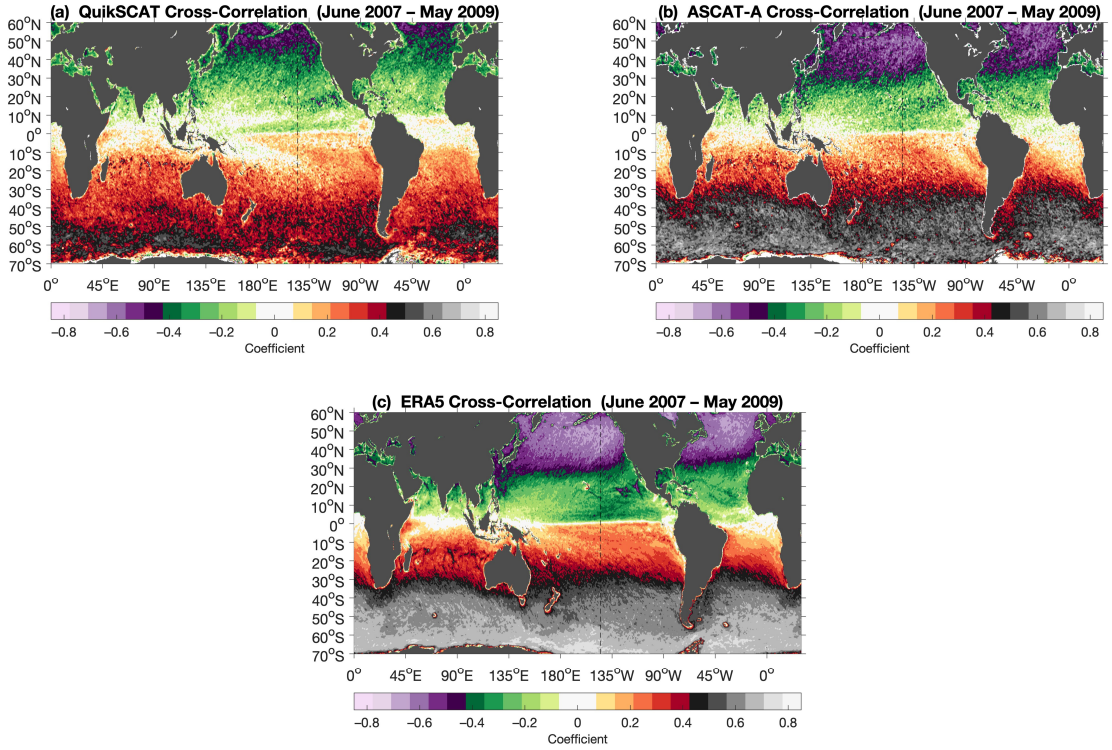

Figure 1. Global divergence and vorticity cross-correlation coefficients calculated for (**a**) QuikSCAT, (**b**) ASCAT-A, and (**c**) ERA5. Calculations used the entire 2-year period between June 2007 and May 2009 and a 1° latitude by 1° longitude-centered window that was varied in latitude/longitude increments of a quarter degree globally. The dashed line is centered at 145°W.

The divergence and vorticity are well correlated over most of the global oceans away from the tropics, and the magnitude of this correlation increases with latitude, as shown in Figure 1. A negative (positive) correlation between divergence and vorticity is observed over the two-year period in the Northern Hemisphere (Southern Hemisphere). This correlation between divergence and vorticity is apparent in QuikSCAT and ASCAT-A scatterometers and from the ERA5 reanalysis, although significant differences in this correlation exist among the three platforms. This is the first report of a cross-correlation between divergence and vorticity over the global oceans and forms the primary motivation for this study. To determine and explain the dynamics of this strong relationship, we exploit the fact that, for much of the time, the steady large-scale surface winds are approximately in steady-state Ekman balance, which is a balance between the pressure gradient, Coriolis, and frictional forces. This dynamical approximation predicts certain properties of the co-variability between the surface divergence and vorticity and variations with latitude, which can be tested using the scatterometer and reanalysis winds.

The primary goal of this research is to statistically describe the co-variability between the surface divergence and vorticity over the global oceans. Further, we seek to develop a mathematical framework for evaluating the statistical distributions of the derivative wind fields using theory, which is presented in Section 2. Finally, we seek to apply this metric for inter-platform comparisons between various satellite scatterometer and numerical weather prediction model wind fields, which are presented in Sections 3 and 4.

2. Methods

We seek to develop a mathematical framework for evaluating the statistical distributions of the divergence and vorticity variability over the ocean from steady-state Ekman dynamics. We hypothesize that Ekman dynamics, which governs the large-scale winds over the ocean, also describe the leading-order dynamics of divergence and vorticity. Steady-state Ekman dynamics is based on a momentum balance (Equation (1)), which includes a frictional term in addition to the pressure gradient and Coriolis terms. This results in a cross-isobar wind vector relative to the sea-level pressure (SLP) isobars, with a component that points from high to low pressure, as shown in Figure 2. Therefore, wind vectors will diverge with anti-cyclonic vorticity out of a high-pressure region and converge with cyclonic vorticity into a low-pressure region [30]. In the mid-latitudes, the average angles between the geostrophic wind vector and the actual wind vector (α) are estimated to be 15°, as used by the Bakun index [31], but these can vary significantly.

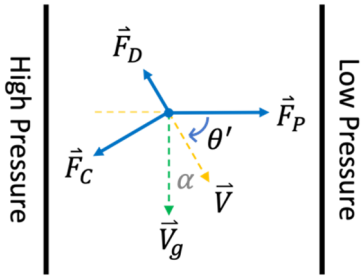

Figure 2. Schematic illustrating the principal force balance associated with steady-state Ekman dynamics in the Northern Hemisphere. In this schematic, the pressure gradient force $(\vec{F}_P)$, drag force $(\vec{F}_D)$, and Coriolis force $(\vec{F}_C)$ are in a balanced state with no net acceleration of the surface air. The angle α is defined as the clockwise angle from the geostrophic wind vector $(\vec{V}_g)$ to the surface wind vector $(\vec{V})$, where the geostrophic wind vector is perpendicular to the pressure gradient force. The angle θ' is defined as the angle from the pressure gradient force vector to the surface wind vector. In this schematic, θ' is negative and between 0° and −90°.

The Equation of horizontal motion at the surface in steady-state Ekman dynamics is written as:

$$f\hat{k} \times \vec{V} + \frac{1}{\rho_o}\vec{\nabla}_H p - \frac{1}{\rho_o}\frac{\partial \vec{\tau}}{\partial z} = 0, \quad (1)$$

where f is the variable Coriolis parameter $f = 2\Omega\sin(\varphi)$, φ is the latitude, $\vec{V}$ is the 10-m horizontal wind vector, $\hat{k}$ is the direction perpendicular to the surface, ρ_o is a constant surface air density, $\vec{\nabla}_H$ is the horizontal del operator, p is the sea-level pressure, $\vec{\tau}$ is the horizontal wind stress vector, and $\frac{\partial}{\partial z}$ is the partial derivative in the $\hat{k}$ direction. The main assumptions applied here from the full Equation of motion include a small Rossby number, steady-state conditions, and no vertical momentum advection.

Following previous work [30,32], we use the standard bulk aerodynamic formula for a well-mixed boundary layer to approximate the vertical turbulent stress divergence at the ocean surface as:

$$\frac{\partial \vec{\tau}}{\partial z} \approx -\frac{\rho_o C_d \left|\vec{V}\right| \vec{V}}{h}, \quad (2)$$

where C_d is the 10 m drag coefficient and h is the Ekman (surface) boundary layer height. This assumption relegates the role of the turbulent stress divergence to surface friction and neglects the possible role of vertical turbulent momentum redistribution from above h to the surface through the entrainment of free-tropospheric air into the boundary layer.

With these assumptions, Equation (1) becomes:

$$f\hat{k} \times \vec{V} + \frac{1}{\rho_o}\vec{\nabla}_H p + \frac{C_d\left|\vec{V}\right|}{h}\vec{V} = 0. \tag{3}$$

Patoux and Brown [32] showed that, by taking the curl of Equation (3), a relationship exists between the ratio of the Coriolis parameter and the surface wind stress (i.e., the magnitude of the drag force) to the ratio of the surface vorticity and divergence:

$$\frac{\hat{k}\cdot\left(\vec{\nabla}_H \times \vec{V}\right)}{\left(\vec{\nabla}_H \cdot \vec{V}\right)} = -\frac{f}{a}, \tag{4}$$

where $a = \frac{C_d|\vec{V}|}{h}$. Given typical mid-latitude oceanic values for wind speed of 7 m s^{-1}, a drag coefficient of 1.4×10^{-3} and an Ekman boundary layer height of 280 m results in $a = 3.5 \times 10^{-5}$ s^{-1}. The Ekman layer depth is often shallower than the more familiar boundary layer depth [33,34]. Note that a term related to the latitudinal gradient of f (i.e., the so-called beta term) is not considered here due to its typically much smaller magnitude compared with the other terms in the expansion. Equation (4) does not restrict the signs of divergence and vorticity individually but only the sign of their ratio. Therefore, in the Northern Hemisphere, given that a is positive-definite and f is positive, there are two possible combinations of vorticity and divergence depending on their sign, each consistent with winds in steady-state Ekman balance: (1) positive divergence and negative vorticity; and (2) convergence and positive vorticity. The converse occurs in the Southern Hemisphere, where f is negative.

Analysis of the vorticity to divergence ratio in Equation (4) becomes difficult when the divergence goes to zero and the ratio becomes undefined. Patoux and Brown [32] examined the mesoscale variance of vorticity to the mesoscale variance in divergence, finding a larger ratio in the mid-latitudes than in the tropics. We, however, developed a method to understand the vorticity to divergence ratio in terms of an angle, which circumvents this singularity issue. The relationship between the divergence and vorticity (Equation (4)) can be expressed as an angle $\alpha\prime$ using Clifford algebra [35]. Clifford algebra, for any two-dimensional vector field, is used to express the spatial derivative of the wind vector ($\vec{\nabla}_H\vec{V}$) as the complex sum of divergence and vorticity (Equation (5)). When expressed in polar form (Figure 3a), the relationship between vorticity and divergence becomes

$$\vec{\nabla}_H\vec{V} = \left(\vec{\nabla}_H\cdot\vec{V}\right) + \left(\vec{\nabla}_H \bigwedge \vec{V}\right) \Rightarrow \left(\vec{\nabla}_H\cdot\vec{V}\right) + i\left[\hat{k}\cdot\left(\vec{\nabla}_H \times \vec{V}\right)\right] = Me^{i\alpha'}, \tag{5}$$

where

$$\alpha' = \tan^{-1}\left(\frac{\hat{k}\cdot\left(\vec{\nabla}_H \times \vec{V}\right)}{\left(\vec{\nabla}_H\cdot\vec{V}\right)}\right), \tag{6}$$

$$M = \sqrt{\left|\vec{\nabla}_H\cdot\vec{V}\right|^2 + \left|\hat{k}\cdot\left(\vec{\nabla}_H \times \vec{V}\right)\right|^2}. \tag{7}$$

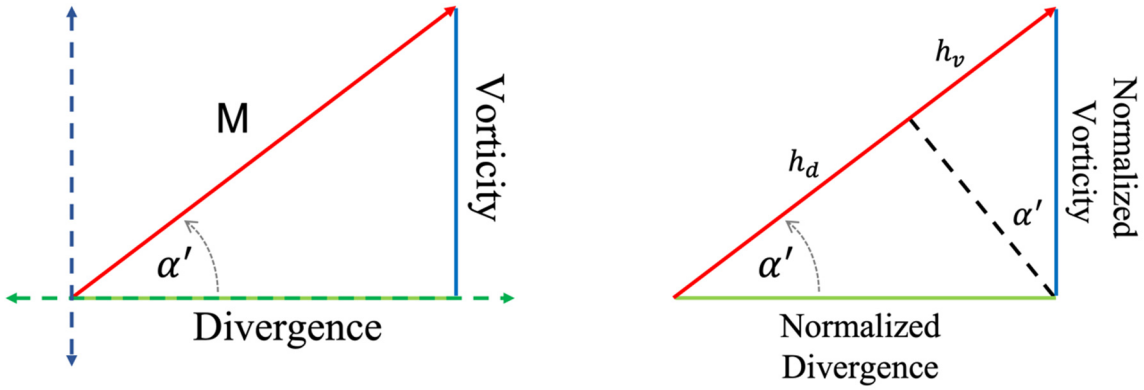

(**a**) (**b**)

Figure 3. (**a**) Diagram of the polar representation of vorticity and divergence in the complex plane. In this schematic, M is the radial magnitude of divergence and vorticity and α' is their direction. (**b**) Diagram of the normalized vorticity and divergence projected onto a unit vector pointing in the direction of α' (Equation (9)).

Thus, combining Equations (4) and (6) results in the following expression, which alleviates the singularity issue of zero divergence in the ratio in Equation (4):

$$\alpha' = \tan^{-1}\left(\frac{\hat{k}\cdot\left(\vec{\nabla}_H \times \vec{V}\right)}{\left(\vec{\nabla}_H \cdot \vec{V}\right)}\right) = \tan^{-1}\left(-\frac{f}{a}\right). \tag{8}$$

Equation (8) implies that steady-state Ekman balanced flow in the Northern Hemisphere can be either anti-cyclonic with diverging winds $(0° \leq \alpha' \leq -90°)$ or cyclonic with converging winds $(90° \leq \alpha' \leq 180°)$. As stated earlier, we exploit the fact that, on average, the steady large-scale surface winds are approximately in steady-state Ekman balance. Therefore, we expect to statistically find most of the surface winds to be in one of these two states.

Angular dependent relationships like Equation (8) have been studied before, by analyzing relationships between the sea surface temperature gradient (SST) and wind stress [21] as well as coupling the natural components of SST and natural components of the wind vectors [36]. However, in this work, the angular dependence between divergence and vorticity is derived directly from Ekman dynamics.

This representation of vorticity and divergence in the complex plane is used here to provide a more rigorous framework to analyze the coupled relationship between divergence (real axis) and vorticity (imaginary axis) given an Ekman balanced state (Figure 3). The proportions of the normalized divergence and vorticity (Equation (9)) can be analyzed by looking at their projection on a unit vector pointing in the direction of α' (Figure 3b), which is also equal to the Pythagorean identity $\sin^2(\alpha') + \cos^2(\alpha') = 1$. These proportions can be used to determine how much the divergence and vorticity contribute individually to an α' probability distribution. These proportions of the unit vector are:

$$h_d + h_v = 1, \tag{9}$$

where h_D and h_V are the projections of the normalized divergence and vorticity components respectively:

$$h_d = \frac{\left(\vec{\nabla}_H \cdot \vec{V}\right)}{M}\cos(\alpha') = \cos^2(\alpha'),$$

$$h_v = \frac{\hat{k} \cdot \left(\vec{\nabla}_H \times \vec{V} \right)}{M} \sin(\alpha') = \sin^2(\alpha').$$

It is also possible to conceptually interpret α' similarly to [30,32] using a point particle model (sum of forces at a point) to solve for the angle of the wind vector using Equation (1) and Figure 2 under steady-state conditions. In this framework, the angle α to the wind vector is calculated relative to the geostrophic wind vector, which is defined conventionally as $(\vec{V}_g = \hat{k} \times \frac{1}{\rho_o f} \vec{\nabla} p)$. In contrast, we define the angle (θ') relative to the pressure gradient as shown in Figure 2. When the along-isobar acceleration is zero, the angle θ' is calculated as the negative ratio of the magnitude of the Coriolis force over the magnitude of the drag force:

$$\theta' = \tan^{-1}\left(-\frac{\left| \vec{F}_C \right|}{\left| \vec{F}_D \right|} \right) = \tan^{-1}\left(-\frac{f}{a} \right). \tag{10}$$

Defining θ' in this way allows for a continuous transition across the equator and is not affected by the Coriolis parameter going to zero at the equator. However, interpreting the angle θ' in this way, i.e., schematically from a point particle model, creates some challenges. The first is that only the forces in the direction of the geostrophic wind (along-isobar) are required to follow steady-state conditions since the cross-isobar acceleration can be non-zero. Secondly, the point particle model is independent of the neighboring data points, and therefore θ' does not equal α', which makes understanding the allowable angles of α' derived from vorticity and divergence in an Ekman balanced framework difficult. This is especially true for converging winds with positive vorticity (angles between 90° and 180° in the Northern Hemisphere), where wind vectors still point from high to low pressure. Comparison of the pressure Laplacian $\left(\nabla^2 p\right)$ with α' is used in Section 4.2 to analyze this point particle model.

The primary advantage of using our α' metric is that flow characteristics can be assessed from the surface wind fields alone without explicit knowledge of the complete horizontal sea-level pressure gradient field, which is largely unknown from observations. This allows us to assess from the observed horizontal wind fields alone whether the correlation between divergence and vorticity observed in Figure 1 is consistent with steady-state Ekman dynamics. One disadvantage of using Equation (8) for this purpose is that comparison of the ratio of vorticity to divergence to the ratio f/a depends on the boundary layer or Ekman layer height in the parameter a, which is a poorly observed quantity, highly variable [37,38], and often ambiguous, particularly in stable stratification or when multiple layers are present [39]. Additionally, the Ekman layer depth and boundary layer depth do not often coincide [33,34], and, thus, estimates of boundary layer depth for this purpose lead to uncertainties in the value of a.

3. Data

This study utilized scatterometer all-weather (AW) 10 m equivalent neutral wind vectors from QuikSCAT and the Advanced Scatterometer on the Metop-A satellite (ASCAT-A). The versions we used were the QuikSCAT v4.1 and the ASCAT-A 25 km products disseminated through the JPL Physical Oceanography Distributed Active Archive Center (PO.DAAC) [40,41] (SeaPAC 2018, EUMETSAT/OSI SAF 2010). We also utilized hourly instantaneous 10 m stress-equivalent neutral wind vectors and sea-level pressure from the Fifth Generation of the European Centre for Medium-Range Weather Forecast (ECWMF) Global Reanalysis [42,43] (ERA5; Copernicus Climate Change Service 2017; Hersbach et al., 2020). The scatterometer wind vectors were provided in swath-level Level 2B (L2B) format at a nominal 12.5 km spacing. The L2B vector winds were gridded onto a uniform 0.25° latitude/longitude grid using a two-dimensional loess smoother [44,45] with a 60 km half-power point. The ERA5 reanalysis of 10-m equivalent neutral winds

was already available on the same 0.25° spatial grid as the gridded scatterometer winds in hourly increments. A subset of the ERA5 hourly data was used that consisted of data at 6-hourly intervals. Thus, wind vectors for all the datasets utilized the same uniform 0.25° latitude/longitude grid. The divergence and vorticity were then computed for all three datasets using conventional second-order-accurate centered finite differences in the wind vector components. Following [3,4], the spatial derivatives for the scatterometer wind fields were computed within each swath.

We focused the analysis in this study on regions spanning 10° longitude by 10° latitude. A fixed 10° longitudinal region of the Pacific Ocean, spanning longitudes between 140°W and 150°W, is the primary location used for the metric development presented here. This longitudinal region is then analyzed by varying the 10° latitudinal region in 1° increments between 60°S and 55°N. Our calculations used 3-month time periods, typically December 2007–February 2008 (DJF 2008), which spanned a period in which QuikSCAT and ASCAT-A operated together. Unless otherwise indicated, no time averaging was applied to any of the fields used in this analysis.

Scatterometer winds are now calibrated to the so-called 10 m stress-equivalent neutral winds (SEW) [46] since scatterometer backscatter measurements respond to the surface wind stress. Given that the surface wind stress depends on the near-surface wind speed, stability, and air density, the SEW is the 10 m wind that would be observed under neutrally stable conditions using a constant air density. A second retrieval quantity that has been used previously for scatterometer wind retrievals is called the 10 m equivalent neutral winds (ENW) [1,46–48] and is similar to the SEW, except that it allows for surface air density variations. The results of this analysis are not sensitive to differences among the ENW, SEW, and the actual 10 m winds from ERA5.

4. Results

4.1. Divergence and Vorticity Probability Distributions

We begin by presenting perhaps the simplest statistical characterization of the divergence and vorticity variability over the oceans, the univariate Probability Density Function (PDF) (Figure 4). In the extratropics, the univariate divergence and vorticity PDFs are characterized by highly skewed distributions, with the PDFs skewed toward cyclonic, convergent winds. The skewnesses result from a preference for higher-amplitude convergent and cyclonic wind events associated with extratropical cyclones and atmospheric fronts [1,8,16,19,49]. The modes of the PDFs consist of weakly divergent and anti-cyclonic winds. It is not possible to ascertain a relationship between the surface winds and Ekman dynamics from just the univariate divergence and vorticity PDFs shown in Figure 4a,b. Steady-state Ekman dynamics predicts a negative correlation between the surface divergence and vorticity in the Northern Hemisphere (NH), where the Coriolis force is positive (see Equation (4)). However, the predicted negative correlation between divergence and vorticity in the NH becomes apparent visually in the joint divergent/vorticity PDFs, for instance, when computed in the Pacific Ocean at 40°N to 50°N (Figure 5a,c,e). Skewnesses in the univariate PDFs apparent in Figure 4 result in an elliptic or comma-shaped joint divergence–vorticity PDF in the mid-latitudes in Figure 5.

The joint PDFs in Figure 5 show that divergence and vorticity are well correlated with each other in the mid-latitudes (also apparent in Figure 1) but have low covariance in the tropics. The joint PDFs also show an approximate elliptic distribution in the tropics and extratropics for the scatterometer and the reanalysis winds. These PDFs indicate that, qualitatively, the divergence–vorticity cross-correlations shown in Figure 1 are not driven by relatively extreme values of either divergence or vorticity. This point is important since we do not expect a steady-state Ekman balance to adequately describe the underlying dynamics for these extreme conditions, which are typical of mid-latitude extratropical cyclones. For the mid-latitude region considered in Figure 5, and for the Rossby number (U/fL) to be much less than 1, the divergence and vorticity—with each scale as U/L, where U is a characteristic velocity scale and L is a characteristic length scale—should

be in the order of 10^{-5} s^{-1}, given that $f \sim 10^{-4}$ s^{-1}. The modes of the divergence and vorticity PDFs are in the order of 10^{-5} s^{-1} and, thus, approximately satisfy the condition of a small Rossby number. The tails of the PDFs have divergence and vorticity values in the order of 10^{-4} s^{-1}, which correspond to a Rossby number of $O(1)$. We thus expect that for these cases, the steady-state Ekman balance inadequately characterizes the surface wind dynamics. Atmospheric frontal regions also likely violate other assumptions of steady-state Ekman dynamics, including significant time-dependent accelerations, entrainment, and large buoyancy-induced vertical velocities. Nonetheless, for these extreme divergence and vorticity values, there is also a strong correlation between divergence and vorticity, mainly for convergent and cyclonic winds. Because these extreme values are much less frequent, we expect that a steady-state Ekman balance will approximately hold for the majority of the individual cases comprising the main body of the divergence–vorticity joint PDF.

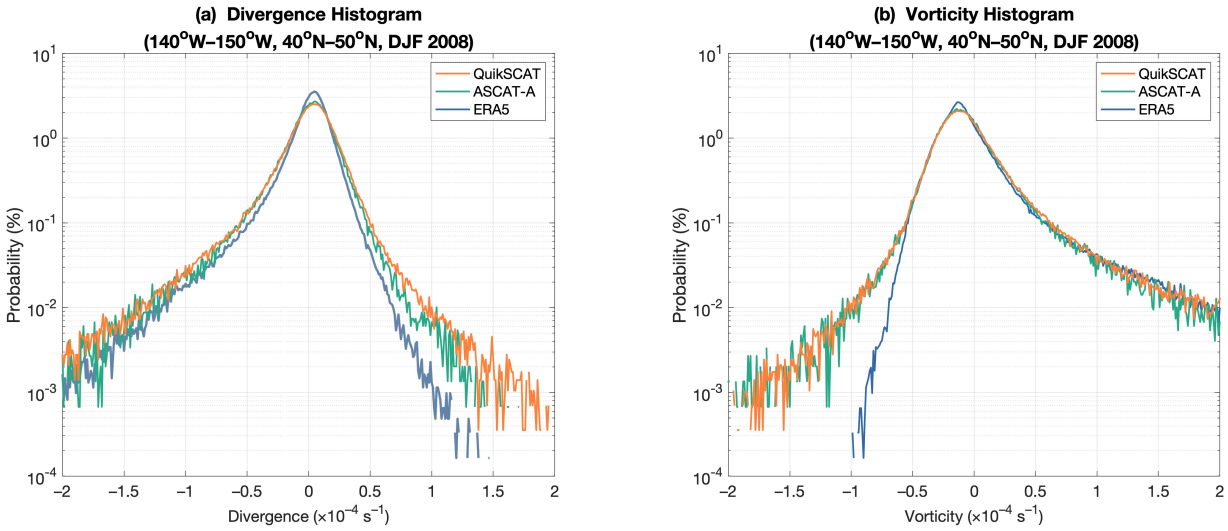

Figure 4. Univariate probability density functions (PDFs) for (**a**) divergence and (**b**) vorticity computed from QuikSCAT (orange), ASCAT-A (green), and ERA5 (blue) for DJF 2008 in the extratropical North Pacific Ocean for the latitude range 40°N–50°N and longitude range 140°W–150°W. A uniform bin width of 1×10^{-6} s^{-1} was used for both the divergence and vorticity. Note the logarithmic scale on the y-axis.

By itself, the vorticity to divergence ratio (Equation (4)) gives insufficient insight into the processes that result in their global variability. This is a result of the many cases where the divergence approaches zero, in which case the ratio of vorticity to divergence becomes undefined. Analyzing the relationship as an angle in polar form, the greatest density of data points in the joint PDF (Figure 6) is observed for α' values between 0° and −90°. The y-axis of Figure 6 shows the radial magnitude (Equation (7)) of the divergence and vorticity. The highest density of points corresponds to a radial magnitude M of about 2×10^{-5} s^{-1}, which is consistent with a small Rossby number and steady-state Ekman balanced flow in the Northern Hemisphere. The strongest radial magnitude values are associated with α' values between 90° and 180°, corresponding with surface convergence and cyclonic vorticity. Balanced flows with a positive divergence and negative vorticity have much smaller radial magnitudes, while balanced flows with convergence and a positive vorticity have a much wider range of possible coupled divergence and vorticity magnitudes, including more occurrences of extreme values. We thus expect these more extreme values to be, on average, associated more with storm systems [8,19].

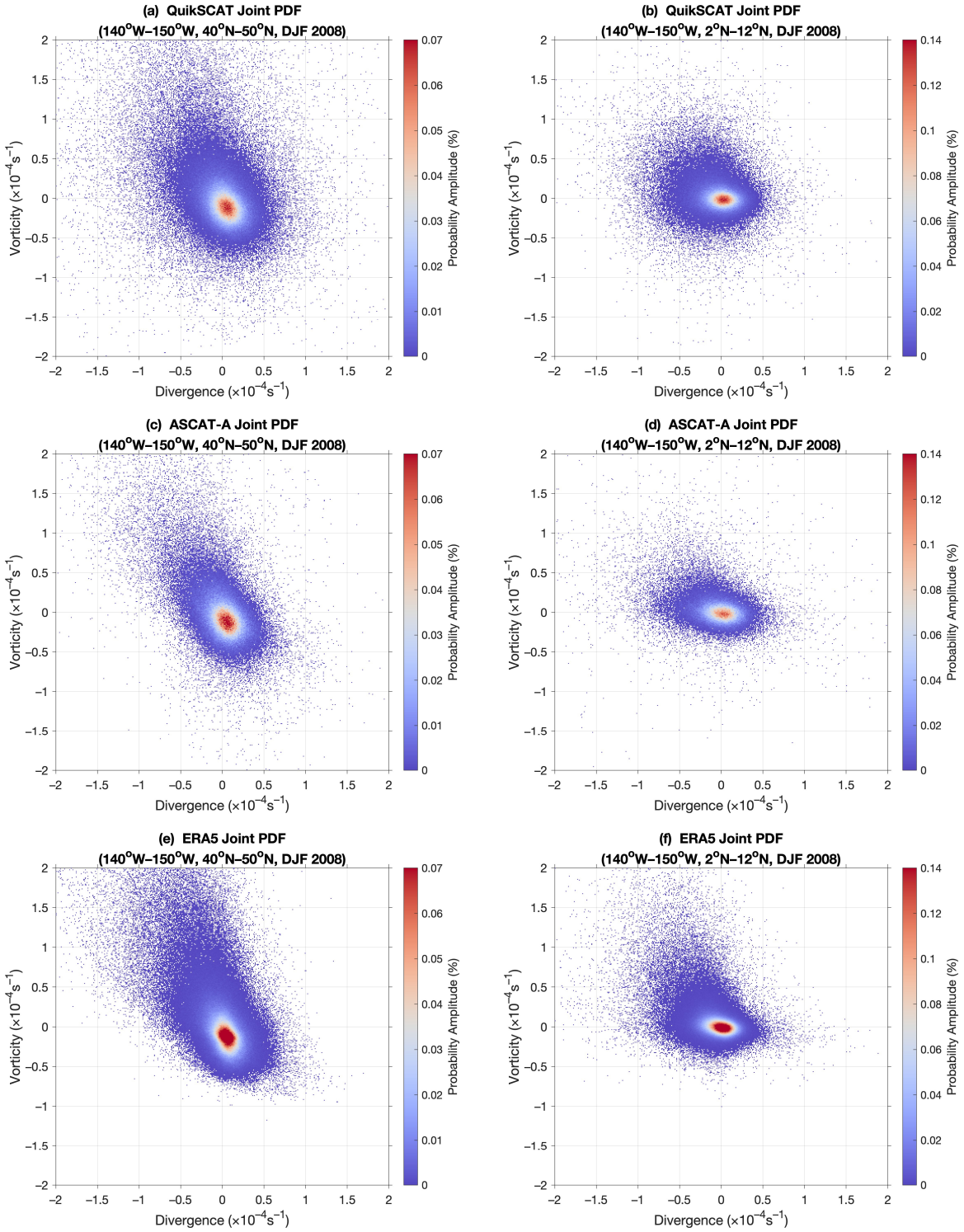

Figure 5. Joint PDFs of the QuikSCAT (**a**,**b**), ASCAT-A (**c**,**d**), and ERA5 (**e**,**f**) divergence (x-axis) and vorticity (y-axis) for DJF 2008 within the longitude range 140°W–150°W and the latitude range between 40°N and 50°N for (**a**,**c**,**e**) and 2°N and 12°N for (**b**,**d**,**f**). A uniform bin width of 1×10^{-6} s^{-1} was used for the joint PDFs.

Steady-state Ekman balanced flow is most simply observed through a univariate PDF of α' (Figure 7), which is calculated from the ocean wind vector's divergence and vorticity using Equation (8). The histograms of α' for the given region and time period were then calculated using a 1° bin width. Smoothed PDF estimates were obtained using

a standard kernel-smoothing function with a bandwidth of 4. Hereafter, peak α' angles and amplitudes are determined from the smoothed PDF. Figure 7 shows that in both the Northern and Southern Hemisphere mid-latitudes, the α' PDFs are bimodal, with a well-defined primary-peak and a smaller amplitude but a well-defined secondary-peak. Wind vectors in balanced flow are identified as the most probable state of the α' PDF. Therefore, the PDF primary-peak corresponds to steady-state conditions of Ekman dynamics under divergent and anti-cyclonic winds, where anti-cyclonic winds correspond to negative vorticity in the Northern Hemisphere and positive vorticity in the Southern Hemisphere. A secondary-peak is often present depending on the latitude, corresponding to convergent and cyclonic winds, which are also consistent with steady-state Ekman dynamics. We discuss the latitudinal variations in the primary- and secondary-peaks further below. The α' PDFs thus show two distinct flow regimes that represent the majority of flow conditions consistent with Ekman dynamics.

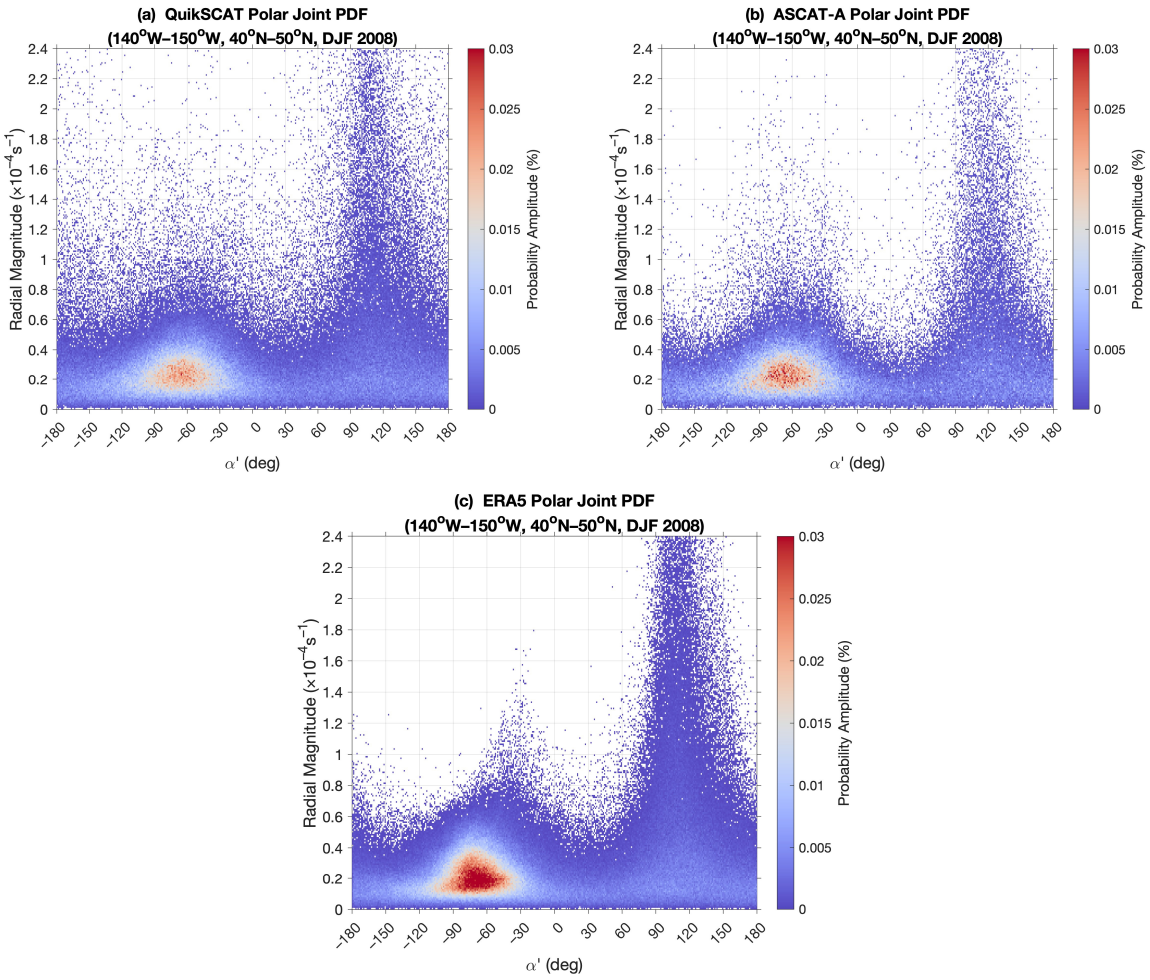

Figure 6. Joint PDF of the radial magnitude of vorticity and divergence (y-axis) and the angle α' (x-axis) from (**a**) QuikSCAT, (**b**) ASCAT-A, and (**c**) ERA5 for the 3-month period DJF 2008 and the region bounded by 140°W–150°W and 40°N–50°N. A uniform bin width of 1×10^{-6} s^{-1} was used in the radial direction together with a 1° angular bin width.

The normalized divergence and vorticity components of the α' PDFs (Figure 8a,b) quantitatively show the coupling of the vorticity and divergence. The components were computed according to the Pythagorean identity as derived in Equation (9). As expected, the primary- and secondary-peaks of Figure 8 show that the divergence–vorticity coupling has a greater vorticity contribution in the mid-latitudes but greater divergence contribution in the tropics. The transition point between the divergence and vorticity contributions to

the primary- and secondary-peaks occurs when the components are equal at $\alpha' = -45°$ in the Northern Hemisphere. A similar result holds for the Southern Hemisphere.

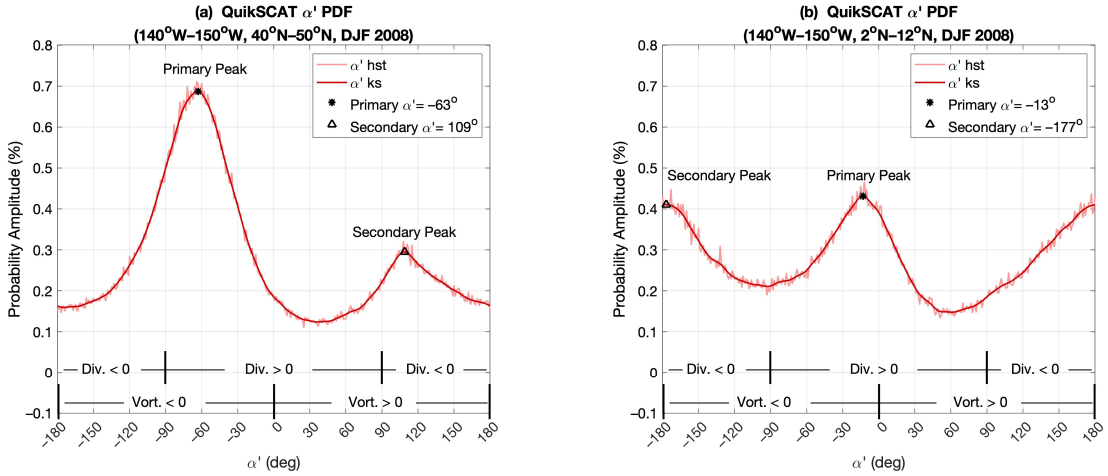

Figure 7. PDFs of the QuikSCAT α' between 140°W to 150°W and (**a**) 40°N to 50°N or (**b**) 2°N to 12°N. The PDFs were computed from instantaneous values over the 3-month period between December 2007 and February 2008. Primary- and secondary-peaks are indicated and correspond to winds consistent with a steady-state Ekman balanced flow. The thin red curves show the unfiltered PDFs, and the thick red curves show the PDFs after low-pass filtering with a kernel-density function as discussed in the text.

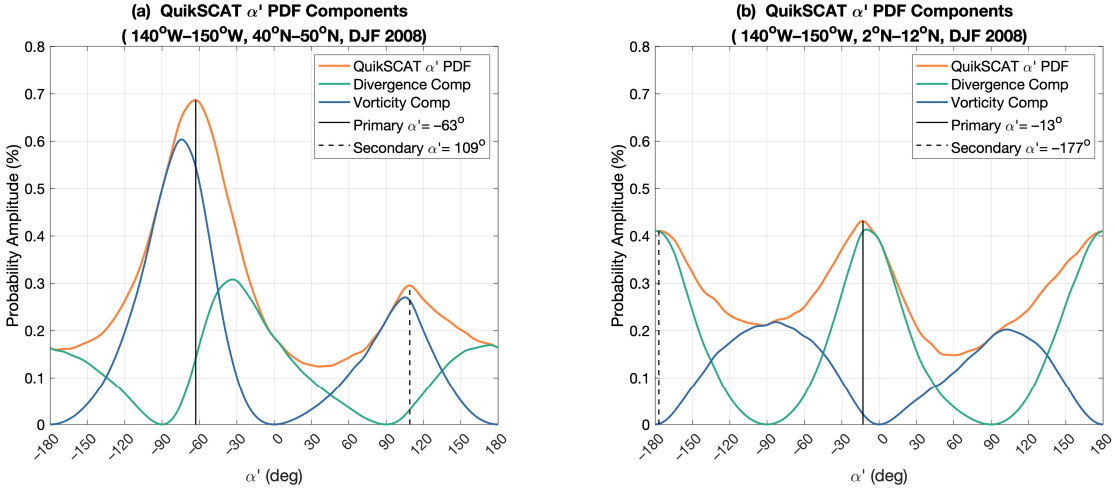

Figure 8. PDFs of the individual projections of the divergence and vorticity to the total α' PDF for (**a**) 40°N to 50°N and (**b**) 2°N to 12°N from QuikSCAT. The green curves show the PDF of the projected divergence component, the blue curves show the PDF of the projected vorticity component, and the orange curves show the total α' PDF. The solid black vertical lines delineate the α' values for the maximum of the primary-peak, and the dashed black vertical line delineates the α' values for the maximum of the secondary-peak. The PDFs were computed from instantaneous divergence and vorticity values over the 3-month period between December 2008 and February 2009.

Similar α' PDFs are observed between different datasets as shown in Figure 9. The QuikSCAT and ASCAT-A scatterometers have good agreement of their α' PDFs in the mid-latitudes, while ERA5 has larger and narrower primary and secondary α' peaks. However, in the tropics, ERA5 and ASCAT-A are in good agreement, while QuikSCAT has a lower secondary-peak amplitude.

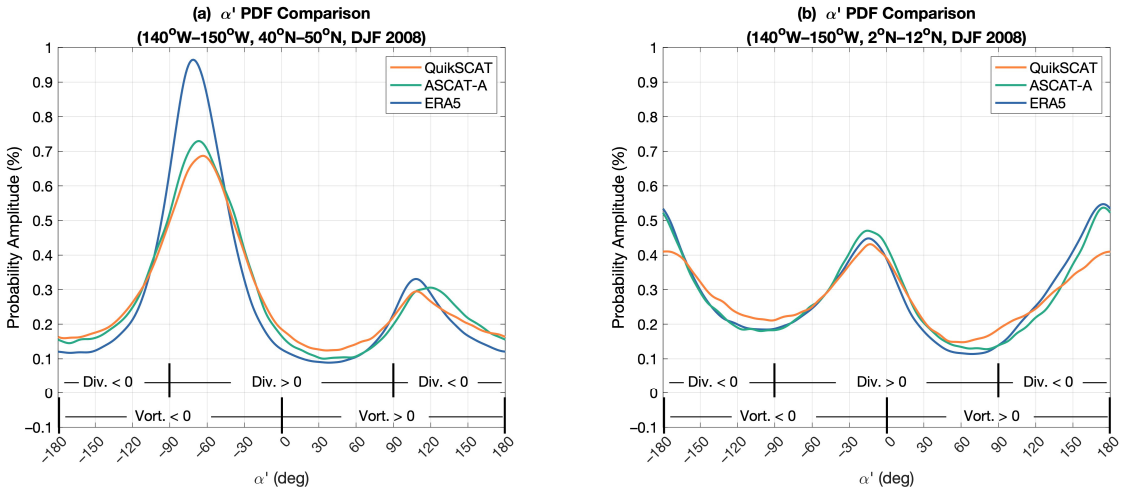

Figure 9. PDFs of α' from QuikSCAT (orange curves), ASCAT-A (green curves), and ERA5 (blue curves) for (**a**) 40°N to 50°N and (**b**) 2°N to 12°N during DJF 2008.

A symmetric latitudinal relationship can be observed when converting the α' PDF into polar form for 10° latitudinal bands between 140°W to 150°W (Figure 10). The polar α' PDF also demonstrates the negative correlation between divergence and vorticity in the Northern Hemisphere and the positive correlation in the Southern Hemisphere that is observed in Figure 1. The strong correlation in the mid-latitudes is a result of the strong covariance between divergence and vorticity, with low covariance observed in the tropics. The correlation persists through the extreme values associated with storm systems.

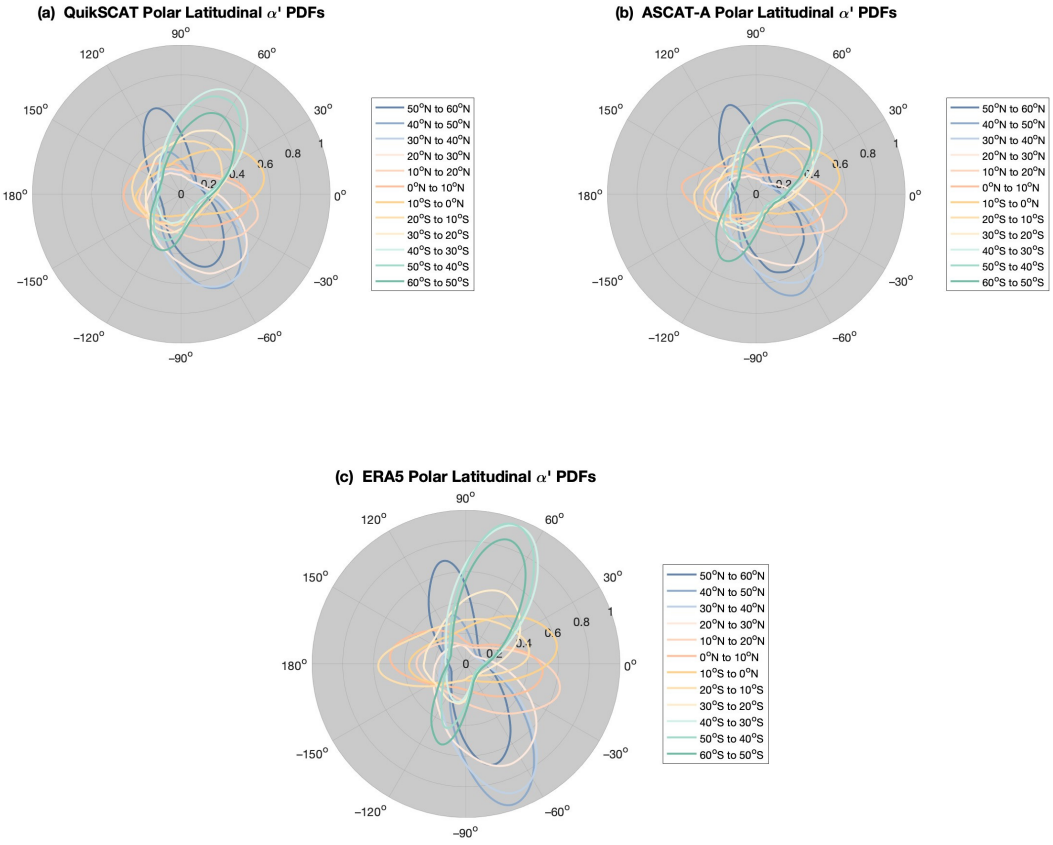

Figure 10. PDFs of α' presented in a polar coordinate system from (**a**) QuikSCAT, (**b**) ASCAT-A, and (**c**) ERA5 for 10° latitude bands between 140°W to 150°W. The radial direction corresponds with the probability amplitude while the angular coordinate corresponds with the angle α'.

4.2. Correlation of α' and Pressure

The primary- and secondary-peaks of the α' PDFs are the most probable states of the surface derivative wind fields. Various distinct atmospheric conditions are aggregated into the PDFs, although we show that the primary- and secondary-peaks are associated principally with larger-scale atmospheric pressure systems. A sample of the various atmospheric states associated with α' regimes are shown in an example map of instantaneous α' angles calculated from Equation (8) for the Pacific Ocean at 12 Z on 30 December 2007 in Figure 11 and a smaller region in Figure 12. Mid-latitude high-pressure regions in the Northern Hemisphere coincide predominantly with α' angles near $-70°$ (orange hue), while Southern Hemispheric high-pressure regions coincide with α' angles near $70°$ (yellow hue). In contrast, the α' angles associated with mid-latitude low-pressure regions of $110°$ NH ($-110°$ SH) are shifted by nearly $180°$ relative to those in high-pressure systems.

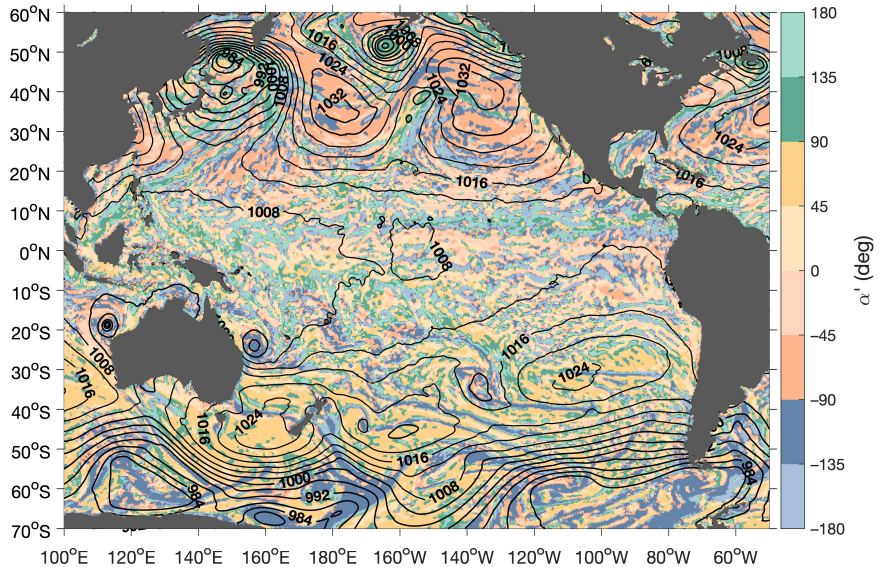

Figure 11. Map of the α' field (shading) calculated from the ERA5 instantaneous wind vector data over the Pacific Ocean from 30 December 2007. The black contours show the ERA5 sea-level pressure in hPa, with a contour interval of 4 hPa. Darker shading emphasizes the vorticity while lighter shading emphasizes the divergence.

Anti-cyclonic winds are observed around the North Pacific Subtropical High in Figure 12 while cyclonic winds occur around the low-pressure region in the Gulf of Alaska. The α' PDF of the region and at the instantaneous time shown in Figure 12 (upper left corner) has a primary-peak angle of $-63°$ and a secondary-peak angle of $103°$. We conclude from the α' PDF that, in the mid-latitudes, the larger spatial scale and higher frequency of occurrence of the high-pressure regions increase the probability amplitude of the primary-peaks relative to the secondary-peaks. Given this characteristic, in general, the primary- and secondary-peaks of α' PDFs reflect the proportion of relative high-pressure areas to the relative low-pressure areas in a region to first order, consistent with the behavior expected from steady-state Ekman dynamics.

Peak probability amplitudes provide a measure of the proportion of high pressure to low pressure in a region through steady-state Ekman dynamics. The ERA5 data provides a way to test the validity of our proposed relationships between the surface winds and sea-level pressure gradients given Ekman dynamics. To better understand this relationship, we analyzed the angle α' derived from a point particle model under steady-state conditions (Equation (10)) between the pressure gradient and wind vectors (Figure 2) and define this angle as θ'. This angle is then analyzed as a function of latitude, as seen in Figure 13. Figure 13 shows a narrow symmetric distribution in the mid-latitudes for the angle between the pressure gradient and the ocean wind vectors. Therefore, nearly all individual wind

vectors outside the immediate tropics qualitatively follow the behavior expected from steady-state Ekman dynamics. That is, on average, the surface winds blow with a component pointing from high to low pressure with a peak θ' angle near $-75°$ (NH), consistent with the average value used by the Bakun index (15° relative to SLP isobars). Unfortunately, the angles in Figure 13 do not describe how the neighboring wind vectors are changing and therefore cannot distinguish between the two possible steady-state regimes predicted from Equation (8).

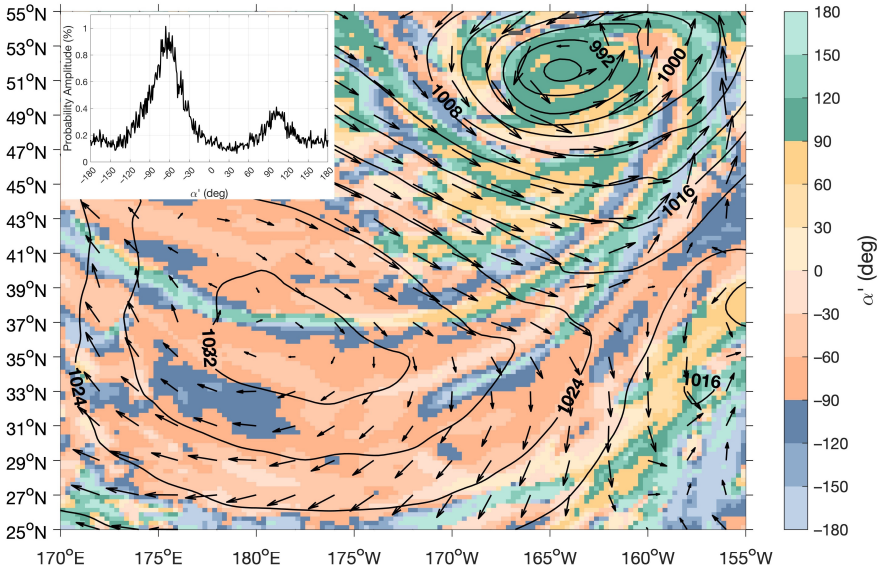

Figure 12. Instantaneous map of the α' angles (shading) calculated from the ERA5 wind vector data (black arrows) over the North Pacific Ocean from 30 December 2007. The sea-level pressure in hPa is indicated with black contours at intervals of 4 hPa. The α' PDF of the region at this time is shown in the inset in the upper left corner. Darker blue/green shading emphasizes the vorticity while lighter orange/red shading emphasizes the divergence. Wind vectors are plotted at 1° latitude/longitude intervals for clarity.

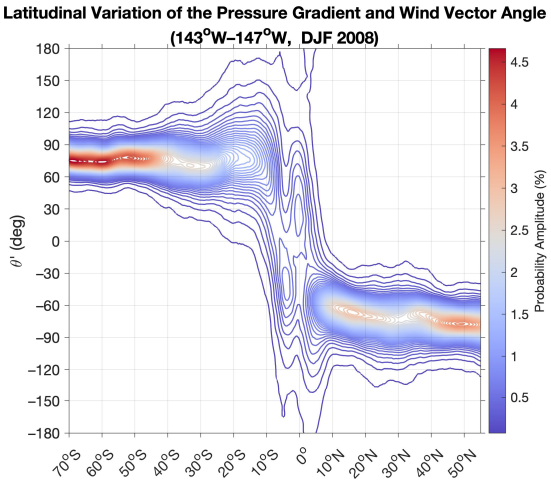

Figure 13. PDF of the angle between the pressure gradient and 10 m wind vectors as a function of latitude from ERA5 for the period DJF 2008.

The pressure Laplacian from ERA5 is used to understand how the change in the neighboring wind vectors relates to the spatial change in the neighboring pressure gradient. Because the angle between the pressure gradient and the wind vector is consistent (Figure 13, mid-latitudes), when the wind vectors diverge or converge, so too should the

pressure gradient vectors. Joint histograms of α' and the pressure Laplacian are shown in Figure 14, where relationships between diverging (converging) wind vectors and pressure Laplacian are observed. The black curve in Figure 14 is a calculation of the mean pressure Laplacian for each α', which shows that diverging (converging) wind vectors are coupled with diverging (converging) pressure gradients. Latitudinal variations in the pressure Laplacian shows higher amplitude pressure Laplacian values in the mid-latitudes and significantly weaker amplitude values in the tropics (Figure 15). As expected, diverging winds with a positive pressure Laplacian, on average, have angles between $-90°$ and $90°$ (red shading) while converging winds with a negative pressure Laplacian have angles between $90°$ and $270°$ (blue shading). Figures 14 and 15 are consistent with the relationship observed in Figure 11, where the α' primary- and secondary-peak amplitudes can be used a measure of the proportion of the relative high pressure to the relative low pressure in a region. This also explains a driving factor for the imbalance of the troughs of the α' PDFs (i.e., Figures 7 and 12). For example, in the α' PDF in Figure 12, there is a higher frequency of high-pressure (primary-peak) to low-pressure (secondary-peak) connections through negative pressures Laplacian (converging winds).

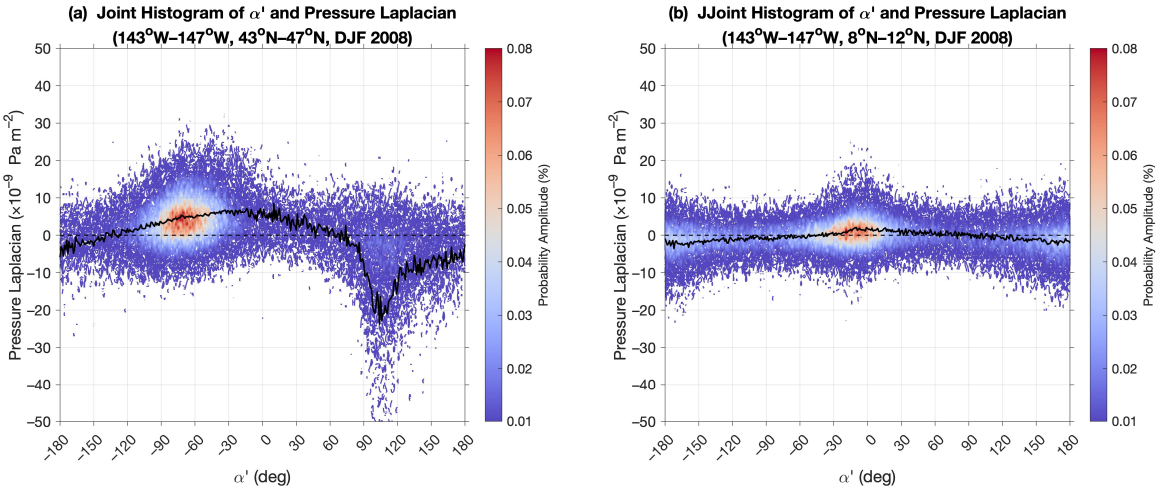

Figure 14. Joint PDFs of α' and the sea-level pressure Laplacian for (**a**) 43°N to 47°N and (**b**) 8°N to 12°N computed from ERA5. The mean pressure Laplacian within each α' bin is indicated by the solid black curves and the zero pressure Laplacian by the black dashed lines.

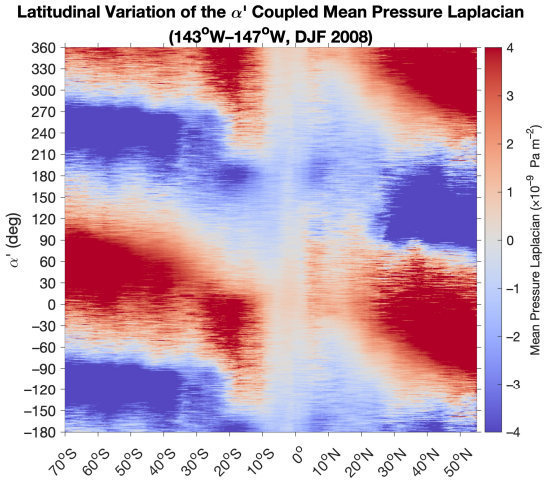

Figure 15. Latitudinal variation in the sea-level mean pressure Laplacian from ERA5 calculated as a function of α'. The α' angles are repeated past $180°$ to fully visualize both the converging and diverging regions without interruption due to the $360°$ wraparound.

In general, the primary and secondary probability amplitudes can be used as a qualitative measure of the proportion of relative high pressure to the relative low pressure in a region following steady-state Ekman dynamics. However, the simple point particle model relating the wind vector to the geostrophic wind vector [32] does not fully describe the relationship between divergence and vorticity, which made consideration of the pressure Laplacian necessary.

4.3. Latitudinal Probability Distributions

Steady-state Ekman dynamics predicts a latitudinal variation in the co-variability between divergence and vorticity by virtue of the variable Coriolis parameter in Equation (8). Latitudinal variations in the α' PDFs calculated using QuikSCAT, ASCAT-A and ERA5 wind vectors are shown in Figure 16a, 16b, and 16c, respectively. High probability amplitudes with α' between -90° and 90° (and 270° and 450° when accounting for the 360° wraparound) correspond with a balanced flow associated with the primary-peak (i.e., divergent and anti-cyclonic winds), while probability amplitudes with α' between 90° and 270° correspond with a balanced flow associated with the secondary-peak (i.e., convergent and cyclonic winds). This is consistent with the latitudinal SLP Laplacian distribution shown in Figure 15, such that a positive (negative) pressure Laplacian corresponds with the primary-peak (secondary-peak). The latitudinal variations in the α' primary-peak amplitudes approximately follow the expected inverse tangent function predicted by steady-state Ekman dynamics (Equation (8)), as shown by the curves in Figure 16 for three representative values of a.

The approximate location of the ITCZ can be determined from the coarse grid in Figure 16 by determining the location of the minimum of the primary-peak and the maximum of the secondary-peak in the α' distributions. This location is at the dotted line at 7°N for both the QuikSCAT and ASCAT-A scatterometers. However, the location of the ITCZ is at 8°N when determined from the ERA5 winds using this metric. This demonstrates a small but significant difference between the scatterometer and reanalysis data.

The ERA5 time-mean divergence is identified in [15] as being less than ASCAT-A over the subtropical gyres. This study also found that the time-mean stress curl in ERA5 is more cyclonic in the mid-latitudes. While not directly comparable, consistent results are observed in the latitudinal variations in α' shown in Figure 16. For ERA5 to have a similar primary- (secondary) peak probability distribution to the scatterometers, the frequency of divergent (convergent) winds with weak vorticity would need to increase while decreasing the probability of strong vorticity and weak divergence (convergence). The larger a values for ERA5 could imply missing drag [14,15], a lower wind speed, or a greater Ekman layer depth (h), assuming that variations in the air density are small. This may also be an indication of the impact of ocean currents on the scatterometer ENWs that are not present in ERA5.

The latitudinal probability distributions show the inverse tangent relationship predicted by Ekman dynamics. The peak of the distributions break from the expected $\pm 75^\circ$ [31] in the subtropics when $\alpha' = \pm 45^\circ$, which is the transition point between the divergence and vorticity contributions. Comparisons between the scatterometer and reanalysis data show similar distributions, with differences occurring in the primary- and secondary-peak probability amplitudes (Figures 7 and 16). ERA5 has consistently narrower primary- and secondary-peaks compared with the scatterometers. From this, it can be concluded that the ERA5 reanalysis data follows steady-state Ekman dynamics (i.e., a Northern Hemisphere primary-peak between 0° and -90°) more consistently than data from QuikSCAT or ASCAT-A observations, implying that ERA5 has underrepresented processes.

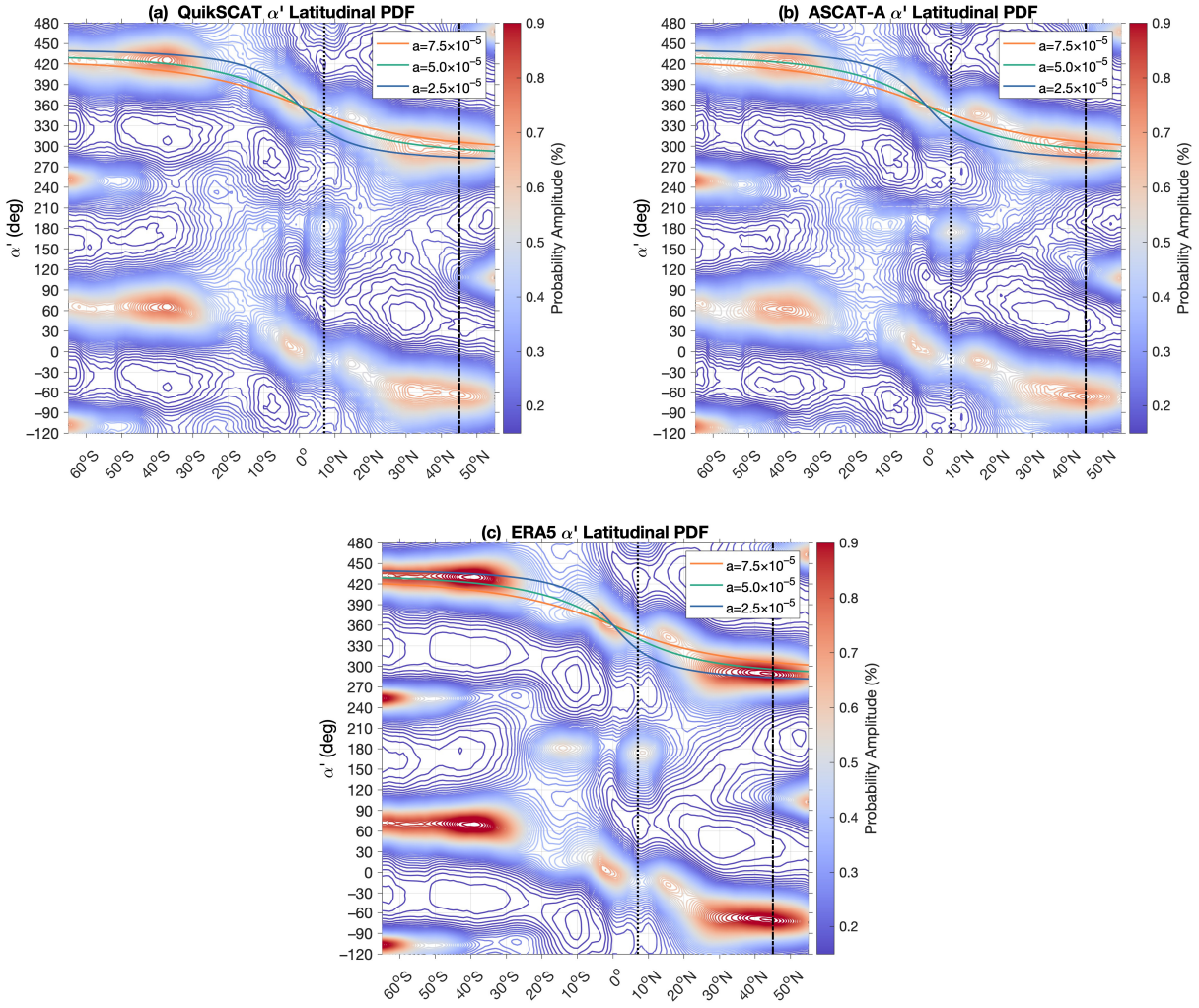

Figure 16. PDFs of α' as a function of latitude between 140°W and 150°W for (**a**) QuikSCAT, (**b**) ASCAT-A, and (**c**) ERA5. The dot–dashed line at 45°N corresponds with the α' PDF calculated between 40°N to 50°N, and the dotted line at 7°N corresponds with the α' PDF calculated between 2°N to 12°N. Note that the α' angles are repeated past 180° to visualize the curves of $\tan^{-1}(-\frac{f}{a})$ at the primary-peak region for three different values of the constant a.

4.4. Seasonal Probability Distributions

The well-defined peaks of the α' PDFs from ERA5 data provide a stronger signal to analyze the α' PDFs. Besides having complete coverage of the region, ERA5 reanalysis fields also provide more temporal data points than the scatterometers, which sample about 1–2 times per day in the mid-latitudes, allowing for more statistical realizations to include in the PDFs. To improve latitudinal resolution of the divergence and vorticity variability, we reduced the spatial extent from which the ERA5 PDFs were computed to 143°W–147°W and used a 4° latitudinal width while keeping the center longitude at 145°W. We continue to use the 4-times-daily ERA5 temporal points, which provide an equivalent number of data points (approx. 100 k) to the scatterometers using a 10° latitude/longitude sampling bin over the same three-month period.

The primary-peaks, associated with α' values between −90° and 90° (270° and 450°), occur more frequently (greater number of black asterisks) than α' values associated with the secondary-peaks (90° to 270°), as shown in Figure 17a–d. The inverse tangent function from Equation (8) with constant values of a is presented for the primary-peak in Figures 17a–d and 18a. As expected, the α' distribution of the primary-peak approximately follows an inverse tangent function as a function of latitude, consistent with the prediction of steady-

state Ekman dynamics. The α' secondary-peak, on the other hand, is observed to have an abrupt transition (seasonally varying) in the transition region between the extratropics and subtropics, which corresponds with wind vectors experiencing either strong vorticity coupled to convergence or strong convergence coupled to vorticity.

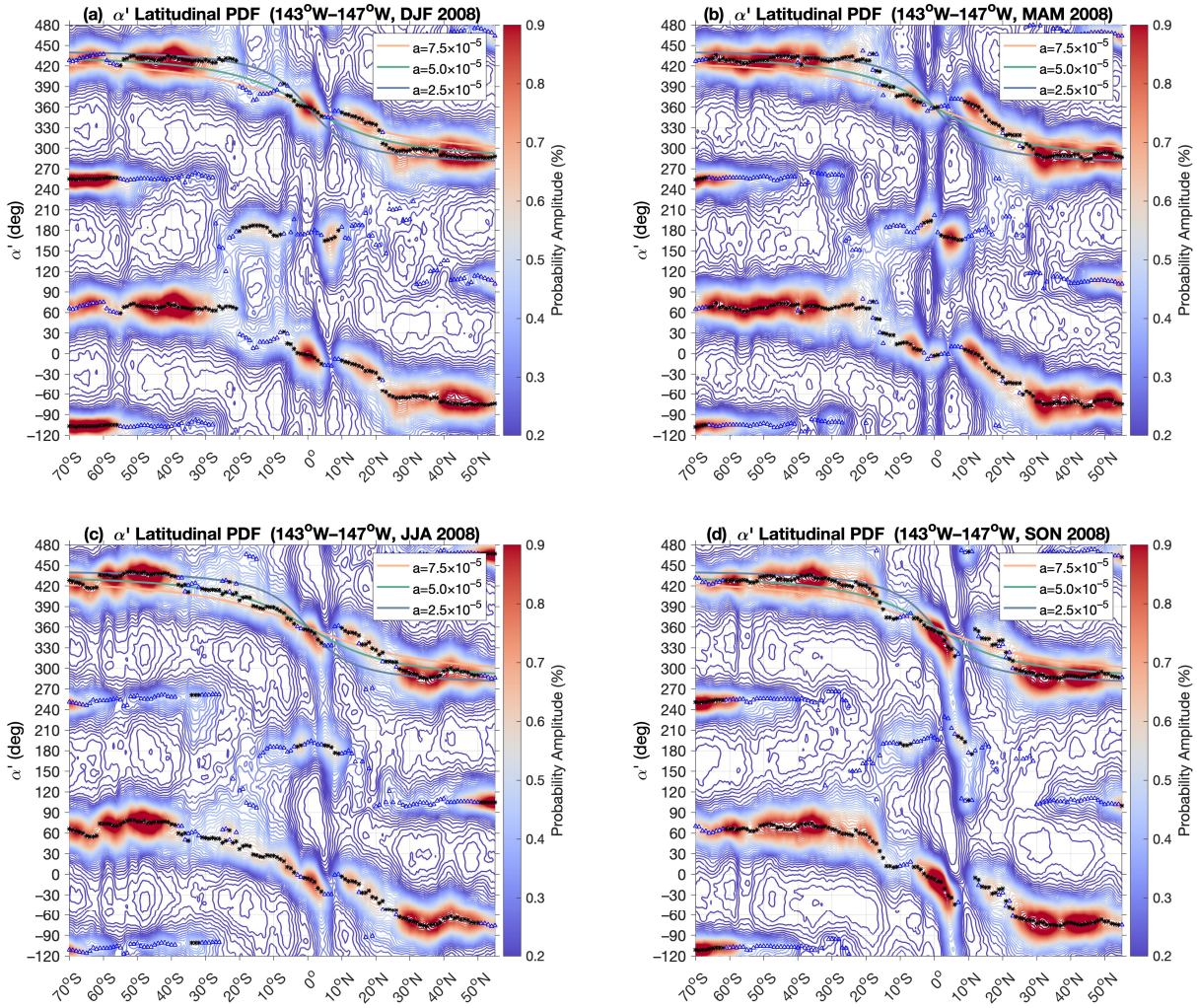

Figure 17. Seasonal variability of the α' PDFs as a function of latitude utilizing ERA5 wind vector data between 143°W to 147°W for the following 3-month periods: (**a**) DJF; (**b**) MAM; (**c**) JJA; (**d**) SON. The highest-amplitude peaks are identified with black asterisks while the second-highest peaks are indicated with blue triangles for a given latitude. Note that the α' angles are repeated past 180° to visualize the curves of $\tan^{-1}(-\frac{f}{a})$ at the primary-peak region for three different values of constant a.

The greatest seasonal variations in the α' PDFs are observed to be associated with the secondary-peak. South of the Pacific Intertropical Convergence Zone (ITCZ), the primary- and secondary-peaks are connected by a large-amplitude negative vorticity peak. For example, in Figure 17b, at 2°S, α' is connected between 180° (secondary-peak) and 360° (primary-peak) by strong negative vorticity. This strong negative vorticity connection varies with the seasonal meridional migration of the ITCZ, which explains the seasonal tropical variation observed in [32]. The vorticity connections north and south of the ITCZ create an offset or shear, with a maximum in SON 2008 and minimum in MAM 2008. A subtle seasonal negative vorticity connection between the ITCZ secondary-peak and approximately 20°N is also present with a corresponding Southern Hemisphere positive vorticity connection. This connection in the subtropics results from the wind field flowing from the subtropical highs toward the ITCZ.

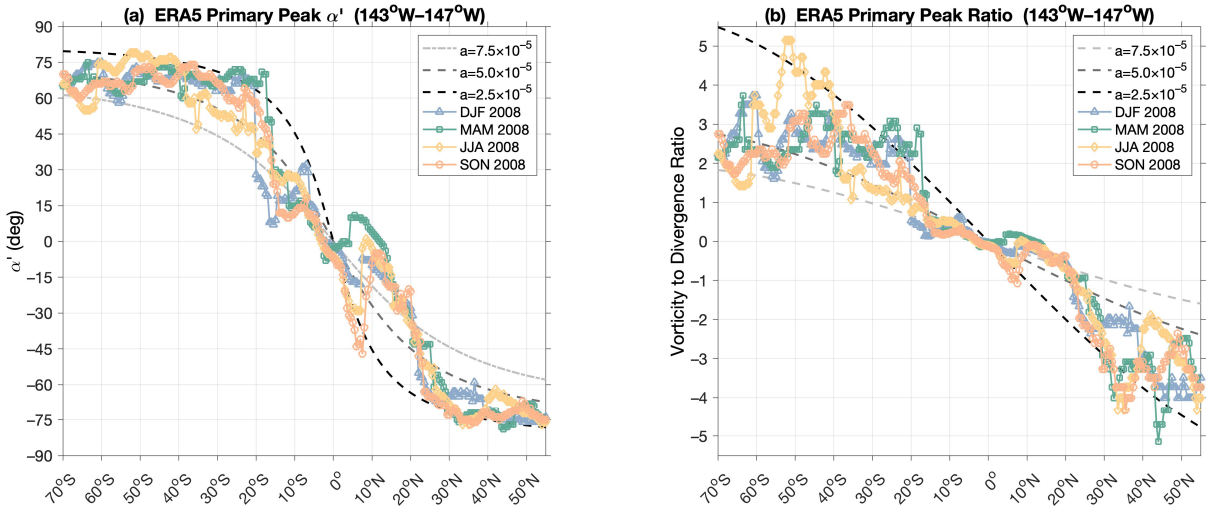

Figure 18. (**a**) Primary-peak angle α' using the ERA5 data according to Equation (8). Dashed curves of $\tan^{-1}(-f/a)$ are presented for constant values of a. (**b**) Vorticity to divergence ratio calculated from the primary-peak angles. Dashed curves of $-f/a$ are presented for three constant values of a.

The inverse tangent function, which describes the location of the primary-peak (Equation (8)), varies the most in the tropics and, as such, amplifies angular changes in the tropics, as seen in Figure 18a, where the latitudinal variation in the primary-peak angle is presented for various seasons in 2008. In contrast, the ratio of vorticity to divergence is more sensitive to variability in the mid-latitudes, as shown in Figure 18b; specifically, for vorticity to divergence ratios greater than plus or minus one ($\alpha' > \pm 45°$). It is possible to convert from α' to the vorticity to divergence ratio using the peak angle (i.e., Equation (8)). Recall that, by themselves, the ratio of vorticity to divergence (Equation (4)) gives insufficient insight into the processes due to the singularity when the divergence goes to zero. The angle α' was therefore calculated to alleviate this discontinuity, and only the α' values corresponding to the peak of the α' PDFs are analyzed. Comparison of Figure 18a,b also shows that the primary-peak is highly variable. However, latitudinal and seasonal variations in the parameter a can nevertheless be obtained. For example, in MAM 2008, south of the ITCZ, the diverging winds of the primary-peak are weakly coupled with negative vorticity, while on the north side of the ITCZ, the wind vectors have positive vorticity, which is not observed during other seasons. Seasonal divergence variations associated with the high-pressure region between 30°N and 40°N (subtropical high) can also be observed (in contrast to [32]). As expected, the divergence is weakly coupled with vorticity during the calmer summer of JJA 2008 and stronger during the winter of DJF 2008. In this case, a is a maximum in DJF and a minimum in JJA. This exemplifies the advantage for our analysis since a is not well known from observations. Analysis of the variation in a as well as utilizing it to analyze entrainment or as an observational constraint for reanalysis data will be left for further investigations.

The latitudinal variation in the primary-peak ratio (Figure 18b) can be used to interpret the latitudinal variation in the correlation coefficients in Figure 1. While not equal, the primary-peak ratio is related to the slope of a simple linear regression between vorticity and divergence, which, in turn, is related to the Pearson correlation coefficient. Therefore, as the primary-peak ratio of vorticity to divergence (slope) goes to zero, so too does the covariance and the correlation coefficient. The latitudinal variation in Figure 18b shows that the correlation coefficient varies approximately with the latitude as $\tan(\alpha')$.

4.5. Global Probability Distributions

We have focused primarily on the Pacific Ocean to develop and establish the utility of the α' metric and to show how steady-state Ekman dynamics can explain much of the statistical variability of surface vorticity and divergence. Global analysis of the coupling between

divergence and vorticity can be achieved by examining the primary- and secondary-peaks in the α' PDFs (Figure 19). The near-global maps on the left (Figure 19a,e,g) show the primary-peak values while the secondary-peak values are observed on the maps on the right (Figure 19d,f,h). The time-mean divergence (Figure 19a) and vorticity (Figure 19b) can help to infer the shape and strength of the primary- and secondary-peaks. For example, the wedge-shaped region of zero vorticity in the tropics (Figure 19b) can be observed in the wedge-shaped primary-peak angle Figure 19e. The spatial structure of the time-mean divergence (Figure 19a) correlates well with that of the primary-peak probability amplitude (Figure 19c) at the equator and ITCZ, but the secondary-peak (Figure 19d) convergent region south of the equator is not as apparent in Figure 19a.

The oceanic western boundary currents are observed as significant variations in peak angles and ratios, as shown in Figure 19e–h, compared with nearby regions with small SST gradients. This results from the atmospheric and surface wind responses to SST gradients, which are known to deviate from a pure steady-state Ekman balance [50–52]. For example, the Gulf Stream is most visible in Figure 19g, where the vorticity to divergence ratio is smaller than that of the surrounding ocean basin. A decrease in the ratio or angle is associated with the less frequent occurrence of negative vorticity and more occurrences of positive divergence in the peak. Mid-latitude variations in α' are best observed in the primary-peak angle, as previously mentioned, while tropical variations in α' are best observed in the vorticity to divergence ratio. We note that air–sea interactions and the surface divergence response to Gulf Stream SST gradients have been investigated previously [52,53], with dynamics consistent with the Ekman balanced model used here.

The $\alpha\prime$ primary-peak probability (high pressure) is greatest in the subtropical oceans around the subtropical highs. In contrast, the secondary-peak probability is greatest at the ITCZ and mid-latitude storm tracks. A global latitudinal symmetry is observed in the secondary-peak probability amplitude (Figure 19d), where the probability amplitude is uniform longitudinally and symmetric in latitude. The primary-peak probability (Figure 19c), on the other hand, shows greater longitudinal variation with increasing probability in the eastern Pacific and Atlantic Oceans.

The large-scale structure of the atmospheric meridional circulation can be observed in the latitudinal variation in the secondary-peak probability amplitude (Figure 19d). The latitudinal circulation transitions can be observed as a measure of the frequency of the relative low-pressure systems (secondary-peak probability). Increased secondary-peak probability around the equator is followed by a low probability at the Hadley–Ferrel cell transition near the 30° latitude and a high probability at the Ferrel–Polar cell transition near the 60° latitude.

Global analyses can be accomplished by examining the primary- and secondary-peak values separately. The components analyzed in Figure 19 demonstrate how steady-state Ekman dynamics governs the large-scale divergence and vorticity variability.

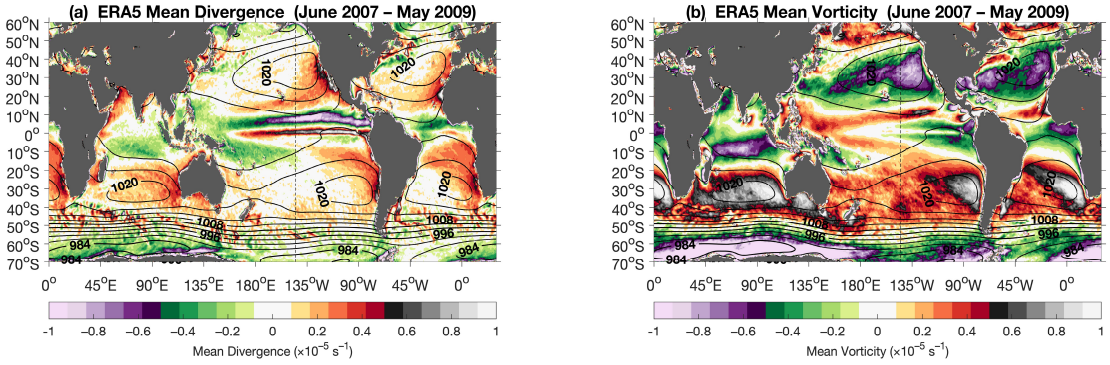

Figure 19. *Cont.*

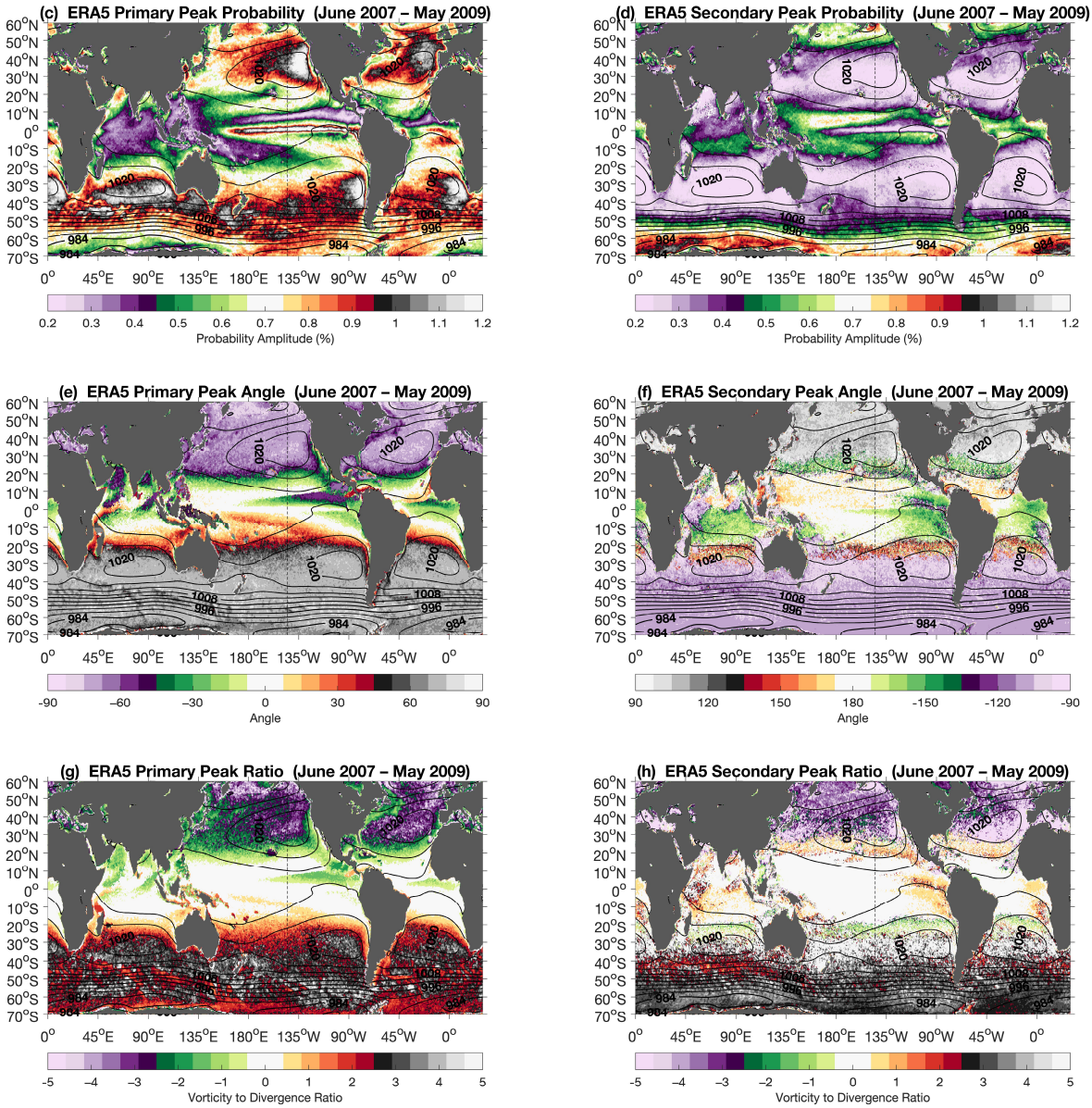

Figure 19. ERA5 global ocean calculations of the (**a**) time-mean divergence, (**b**) time-mean vorticity, (**c**) α' primary-peak probability amplitude, (**d**) α' secondary-peak probability amplitude, (**e**) α' primary-peak angle, (**f**) α' secondary-peak angle, (**g**) α' primary-peak ratio, and (**h**) α' secondary-peak ratio. Calculations used fields for the 2-year period between June 2007 and May 2009 with a 1° latitude by 1° longitude bin width that was varied every quarter degree globally. The time-mean sea-level pressure in hPa is indicated with black contours at intervals of 4 hPa. The dashed line is centered at 145°W.

5. Discussion

This work explains the correlation between divergence and vorticity over the global oceans, which was shown in Figure 1. The ratio of vorticity to divergence is derived from steady-state Ekman dynamics and shown to be the negative ratio of the Coriolis parameter over the constant a (Equation (4)). Within the framework of steady-state Ekman dynamics, variations in this first-order relationship between the surface divergence and vorticity can be explained by the latitudinally varying Coriolis parameter, changes in the boundary layer height component of a, and the surface drag related to the drag coefficient and surface wind speed. The symmetric nature about the equator of the latitudinal relationship between divergence and vorticity is exemplified through polar α' PDFs, i.e., Figure 10. In the North-

ern Hemisphere (i.e., Figure 7), the α' PDF has a primary-peak relating to the maximum probability of divergent winds with negative vorticity (Figure 10; blue distributions).

Our primary hypothesis tested was that the co-variability between surface divergence and vorticity can be described primarily by steady-state Ekman dynamics. The cross-correlation of divergence and vorticity (Figure 1a–c) shows a remarkable relationship, with the strongest correlation at the poles and a hemispherically symmetric latitudinal transition region through the tropics. This relationship correlates with the $\tan(\alpha')$ relationship of the primary-peak vorticity to divergence ratio (Figures 18 and 20). The abrupt change in the correlation coefficient in the extratropics of Figure 1 is also a result of the low covariance observed in Figure 10. The extratropical low covariance correlates with the transition point between divergence and vorticity that defines the dominant contributor to the primary-peak. This transition point occurs when the primary-peak angle $\alpha' = \pm 45^\circ$ or primary-peak ratio $\tan(\alpha') = \pm 1$.

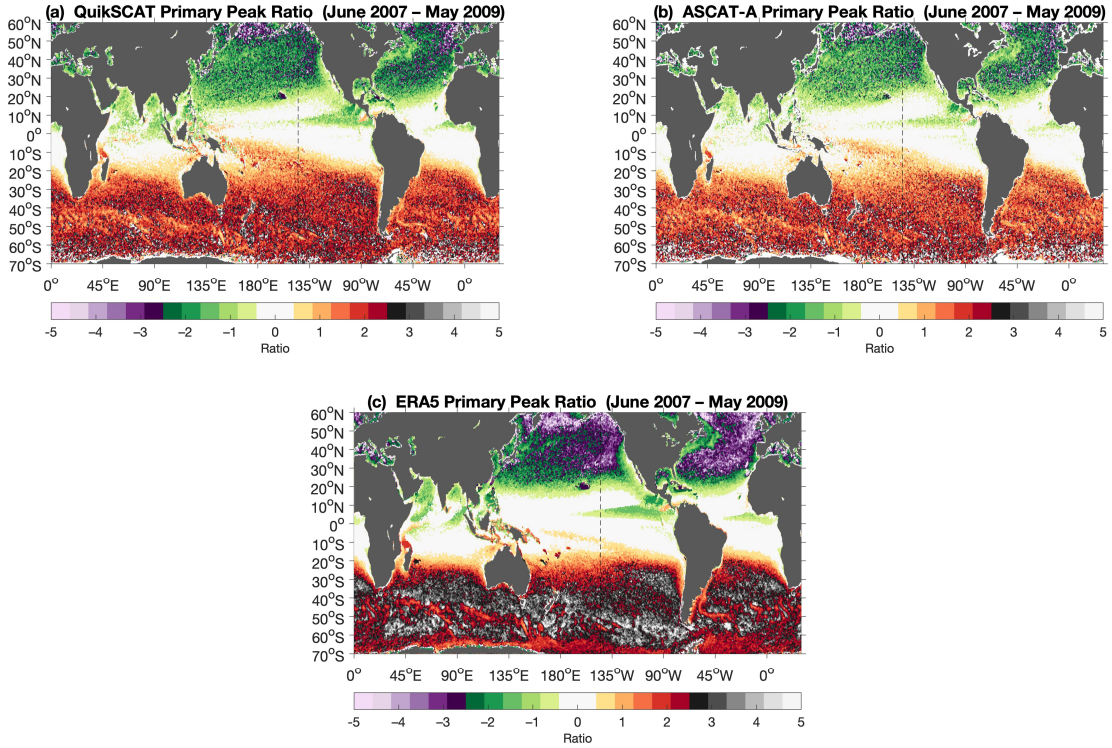

Figure 20. Global primary-peak ratio calculated from the tangent of the α' primary-peak angle for (**a**) QuikSCAT, (**b**) ASCAT-A, and (**c**) ERA5. Calculations used the 2-year period between June 2007 and May 2009 with a 1° latitude by 1° longitude bin width that was varied every quarter degree globally. The dashed line is centered at 145°W.

We used probability amplitudes to compare the ASCAT-A and QuikSCAT scatterometers with ERA5 10 m neutral wind vectors. ERA5 10 m neutral winds have larger primary- and secondary-peak amplitudes in the α' PDFs and narrower PDF peaks in the mid-latitudes when compared with the satellite scatterometers (Figure 16). This indicates that ERA5 more consistently follows steady-state Ekman dynamics. When comparing ASCAT-A and QuikSCAT, the largest difference in the probability distribution is in the secondary-peak. The secondary-peak of QuikSCAT in the tropics is markedly reduced when compared with ASCAT-A and ERA5. We hypothesize that this may result from scatterometer observational errors and higher uncertainties in the QuikSCAT winds in rain, which are often associated with conditions accompanying convergent winds. This hypothesis warrants further investigation. Additionally, we suspect that differences in the horizontal resolution and temporal sampling also contribute to differences in the divergence and vorticity fields among the three datasets. We are currently investigating these differences in more detail. Regardless,

the new methodology developed here gives us a clear framework and path forward for investigating and interpreting these differences.

The elliptically shaped α' PDFs confirm the antisymmetric angular relationship calculated by [36]. Angular distributions of wind stress vorticity to wind stress divergence (not shown here) have similar distributions to the α' PDFs and indicate a preference for elliptic distributions. To achieve similar results at varying latitudes (not just at the equator [36]), phases and amplitudes similar to [24] should be used for elliptic distributions.

The coupled divergence–vorticity system can be used to improve univariate analysis since divergence and vorticity have significant co-variability, as indicated by the α' PDFs. Extreme weather such as mid-latitude extratropical cyclones increase the skewness of the univariate PDFs. Improvements to these previous analyses can be made by damping the extreme divergence and vorticity values associated with storms utilizing a 2-sigma extreme-value filter [25]. This can be further enhanced by filtering the divergence and vorticity joint probability distribution using a Mahalanobis ellipse of distance 2. Such an analysis is subject to future work.

A possible difference in the α' PDFs between scatterometers and ERA5 may be due to surface ocean currents. Scatterometers infer surface winds from surface stress, which is due to the relative motion between the surface wind and ocean currents. ERA5 assumes a stationary surface in the generation of its reanalysis. Ocean surface currents on the spatial scales of scatterometer wind footprints are quasi-geostrophic and, thus, will have a stronger current vorticity relative to its divergence. However, ocean surface currents have strong inertial variability at high frequencies, which adds additional complications to interpreting how spatial variability in ocean currents could affect scatterometer winds relative to reanalysis winds. The ultimate effect that ocean currents have on the α' PDFs is still an open question and will be the subject of future investigation.

Future analysis of the α' PDFs using the divergence and vorticity components in a natural coordinate system is hypothesized to explain the observed differences between scatterometers and NWP reanalysis fields. The vorticity and divergence in natural coordinates are defined in terms of speed and direction components. These components are more applicable to satellite wind retrieval algorithms, as these algorithms explicitly retrieve wind speed and direction rather than vector wind components. Uncertainties in vector wind components are a combination of speed and direction retrieval uncertainties, including random and systematic observational errors, making it difficult to isolate potential deficiencies in scatterometer geophysical model functions. An analysis of the derivative wind fields will then be more likely to lead to a better understanding of the impacts of systematic wind retrieval errors. Finally, practically no methodology, theory, or observational data exist to constrain the statistical distributions of divergence and vorticity. This study provides a pathway to understanding the fundamental characteristics of divergence and vorticity, and their apparent co-variability, over the global oceans.

6. Conclusions

Vorticity and divergence are succinctly correlated to first order through steady-state Ekman dynamics. A correlation between the two is predicted by steady-state Ekman dynamics and was verified here using QuikSCAT, ASCAT-A, and ERA5 ocean wind vector data. The sign of this correlation is dependent on the sign-reversed Coriolis parameter. The α' PDFs are shown to be a novel way to examine the variability and coupling between vorticity and divergence. The α' PDFs of the QuikSCAT and ASCAT-A scatterometers and ERA5 agree well over most regions, with differences in the probability amplitudes resulting from broader scatterometer peak distributions. We use the α' PDFs to verify the latitudinal relationship predicted by Ekman dynamics. Two peaks are found in the α' PDFs: a primary-peak with divergent and anti-cyclonic winds and a secondary-peak with convergent and cyclonic winds. The probability peaks are shown to relate the frequency of relative high pressure and relative low pressure in the region through steady-state Ekman dynamics. Global analyses were accomplished by examining the α' primary- and secondary-

peak values separately and demonstrated how steady-state Ekman dynamics governs the large-scale divergence and vorticity fields. This analysis showed a strong correlation between divergence and vorticity over the global oceans as a significant climatological characteristic of the surface wind fields that, to our knowledge, has not been reported previously. Furthermore, the results show that steady-state Ekman dynamics can explain this observed characteristic to leading order.

Author Contributions: Conceptualization, R.J. and L.W.O.; methodology, R.J.; software, R.J.; validation, R.J. and L.W.O.; formal analysis, R.J.; investigation, R.J.; resources, L.W.O.; data curation, R.J. and L.W.O.; writing—original draft preparation, R.J.; writing—review and editing, R.J. and L.W.O.; visualization, R.J.; supervision, L.W.O.; project administration, L.W.O.; funding acquisition, R.J. and L.W.O. All authors have read and agreed to the published version of the manuscript.

Funding: This research was funded by the National Aeronautics and Space Administration's Future Investigators in NASA Earth and Space Science and Technology; grant number 80NSSC19K1373. L.W.O. was funded in part with funding from the Jet Propulsion Laboratory, California Institute of Technology (contract 1612966), under a grant awarded from the NASA MEASUREs program (NNH17ZDA001N-MEASURES). L.W.O. was also funded in part through NASA grant 80NSSC19K1117 as part of the NASA Physical Oceanography program.

Data Availability Statement: The data presented in the study are available online [40–42].

Conflicts of Interest: The authors declare no conflicts of interest.

References

1. Bourassa, M.A.; Meissner, T.; Cerovecki, I.; Chang, P.S.; Dong, X.; De Chiara, G.; Donlon, C.; Dukhovskoy, D.S.; Elya, J.; Fore, A.; et al. Remotely Sensed Winds and Wind Stresses for Marine Forecasting and Ocean Modeling. *Front. Mar. Sci.* **2019**, *6*, 443. [CrossRef]
2. Chelton, D.B.; Schlax, M.G.; Freilich, M.H.; Milliff, R.F. Satellite Measurements Reveal Persistent Small-Scale Features in Ocean Winds. *Science* **2004**, *303*, 978–983. [CrossRef] [PubMed]
3. O'Neill, L.W.; Haack, T.; Durland, T. Estimation of Time-Averaged Surface Divergence and Vorticity from Satellite Ocean Vector Winds. *J. Clim.* **2015**, *28*, 7596–7620. [CrossRef]
4. Milliff, R.F.; Morzel, J.; Chelton, D.B.; Freilich, M.H. Wind Stress Curl and Wind Stress Divergence Biases from Rain Effects on QSCAT Surface Wind Retrievals. *J. Atmos. Ocean. Technol.* **2004**, *21*, 1216–1231. [CrossRef]
5. Bourassa, M.A.; McBeth Ford, K. Uncertainty in Scatterometer-Derived Vorticity. *J. Atmos. Ocean. Technol.* **2010**, *27*, 594–603. [CrossRef]
6. Back, L.E.; Bretherton, C.S. On the Relationship between SST Gradients, Boundary Layer Winds, and Convergence over the Tropical Oceans. *J. Clim.* **2009**, *22*, 4182–4196. [CrossRef]
7. Back, L.E.; Bretherton, C.S. A Simple Model of Climatological Rainfall and Vertical Motion Patterns over the Tropical Oceans. *J. Clim.* **2009**, *22*, 6477–6497. [CrossRef]
8. King, G.P.; Portabella, M.; Lin, W.; Stoffelen, A. Correlating Extremes in Wind Divergence with Extremes in Rain over the Tropical Atlantic. *Remote Sens.* **2022**, *14*, 1147. [CrossRef]
9. Vogelzang, J.; Stoffelen, A. ASCAT Ultrahigh-Resolution Wind Products on Optimized Grids. *IEEE J. Sel. Top. Appl. Earth Obs. Remote Sens.* **2017**, *10*, 2332–2339. [CrossRef]
10. Vogelzang, J.; Stoffelen, A. On the Accuracy and Consistency of Quintuple Collocation Analysis of in Situ, Scatterometer, and NWP Winds. *Remote Sens.* **2022**, *14*, 4552. [CrossRef]
11. Wang, Z.; Stoffelen, A.; Zou, J.; Lin, W.; Verhoef, A.; Zhang, Y.; He, Y.; Lin, M. Validation of New Sea Surface Wind Products from Scatterometers Onboard the HY-2B and Metop-C Satellites. *IEEE Trans. Geosci. Remote Sens.* **2020**, *58*, 4387–4394. [CrossRef]
12. Weissman, D.E.; Stiles, B.W.; Hristova-Veleva, S.M.; Long, D.G.; Smith, D.K.; Hilburn, K.A.; Jones, W.L. Challenges to Satellite Sensors of Ocean Winds: Addressing Precipitation Effects. *J. Atmos. Ocean. Technol.* **2012**, *29*, 356–374. [CrossRef]
13. Zhao, K.; Stoffelen, A.; Verspeek, J.; Verhoef, A.; Zhao, C. A Conceptual Rain Effect Model for Ku-Band Scatterometers. *IEEE Trans. Geosci. Remote Sens.* **2023**, *61*, 1–9. [CrossRef]
14. Simpson, I.R.; Bacmeister, J.T.; Sandu, I.; Rodwell, M.J. Why Do Modeled and Observed Surface Wind Stress Climatologies Differ in the Trade Wind Regions? *J. Clim.* **2018**, *31*, 491–513. [CrossRef]
15. Belmonte Rivas, M.; Stoffelen, A. Characterizing Era-Interim and ERA5 Surface Wind Biases Using ASCAT. *Ocean Sci.* **2019**, *15*, 831–852. [CrossRef]
16. Zheng, Q.; Yan, X.-H.; Liu, W.T.; Tang, W.; Kurz, D. Seasonal and Interannual Variability of Atmospheric Convergence Zones in the Tropical Pacific Observed with ERS-1 Scatterometer. *Geophys. Res. Lett.* **1997**, *24*, 261–263. [CrossRef]
17. Žagar, N.; Skok, G.; Tribbia, J. Climatology of the ITCZ Derived from ERA Interim Reanalyses. *J. Geophys. Res.* **2011**, *116*, D15. [CrossRef]

18. Grodsky, S.A.; Carton, J.A. The Intertropical Convergence Zone in the South Atlantic and the Equatorial Cold Tongue. *J. Clim.* **2003**, *16*, 723–733. [CrossRef]
19. Liu, W.T.; Xie, X. Double Intertropical Convergence Zones-a New Look Using Scatterometer. *Geophys. Res. Lett.* **2002**, *29*, 29-1–29-4. [CrossRef]
20. Meenu, S.; Rajeev, K.; Parameswaran, K.; Suresh Raju, C. Characteristics of the Double Intertropical Convergence Zone over the Tropical Indian Ocean. *J. Geophys. Res.* **2007**, *112*, D11. [CrossRef]
21. Halpern, D.; Hung, C.-W. Satellite Observations of the Southeast Pacific Intertropical Convergence Zone during 1993–1998. *J. Geophys. Res. Atmos.* **2001**, *106*, 28107–28112. [CrossRef]
22. Luis, A.J.; Pandey, P.C. Characteristics of Atmospheric Divergence and Convergence in the Indian Ocean Inferred from Scatterometer Winds. *Remote Sens. Environ.* **2005**, *97*, 231–237. [CrossRef]
23. Milliff, R.F.; Morzel, J. The Global Distribution of the Time-Average Wind Stress Curl from NSCAT. *J. Atmos. Sci.* **2001**, *58*, 109–131. [CrossRef]
24. O'Neill, L.W.; Chelton, D.B.; Esbensen, S.K. The Effects of SST-Induced Surface Wind Speed and Direction Gradients on Midlatitude Surface Vorticity and Divergence. *J. Clim.* **2010**, *23*, 255–281. [CrossRef]
25. O'Neill, L.W.; Haack, T.; Chelton, D.B.; Skyllingstad, E. The Gulf Stream Convergence Zone in the Time-Mean Winds. *J. Atmos. Sci.* **2017**, *74*, 2383–2412. [CrossRef]
26. Holbach, H.M.; Bourassa, M.A. The Effects of Gap-Wind-Induced Vorticity, the Monsoon Trough, and the ITCZ on East Pacific Tropical Cyclogenesis. *Mon. Weather. Rev.* **2014**, *142*, 1312–1325. [CrossRef]
27. King, G.P.; Vogelzang, J.; Stoffelen, A. Upscale and Downscale Energy Transfer over the Tropical Pacific Revealed by Scatterometer Winds. *J. Geophys. Res. Ocean.* **2015**, *120*, 346–361. [CrossRef]
28. Masunaga, R.; Nakamura, H.; Taguchi, B.; Miyasaka, T. Processes Shaping the Frontal-Scale Time-Mean Surface Wind Convergence Patterns around the Gulf Stream and Agulhas Return Current in Winter. *J. Clim.* **2020**, *33*, 9083–9101. [CrossRef]
29. Wentz, F.J.; Ricciardulli, L.; Rodriguez, E.; Stiles, B.W.; Bourassa, M.A.; Long, D.G.; Hoffman, R.N.; Stoffelen, A.; Verhoef, A.; O'Neill, L.W.; et al. Evaluating and Extending the Ocean Wind Climate Data Record. *IEEE J. Sel. Top. Appl. Earth Obs. Remote Sens.* **2017**, *10*, 2165–2185. [CrossRef]
30. Holton, J.R. *An Introduction to Dynamic Meteorology*; Elsevier Academic Press: Amsterdam, The Netherlands, 2009.
31. Jacox, M.G.; Edwards, C.A.; Hazen, E.L.; Bograd, S.J. Coastal Upwelling Revisited: Ekman, Bakun, and Improved Upwelling Indices for the U.S. West Coast. *J. Geophys. Res. Ocean.* **2018**, *123*, 7332–7350. [CrossRef]
32. Patoux, J.; Brown, R.A. Spectral Analysis of QuikSCAT Surface Winds and Two-Dimensional Turbulence. *J. Geophys. Res. Atmos.* **2001**, *106*, 23995–24005. [CrossRef]
33. Nicholls, S.; Leighton, J. An Observational Study of the Structure of Stratiform Cloud Sheets: Part I. Structure. *Q. J. R. Meteorol. Soc.* **1986**, *112*, 431–460. [CrossRef]
34. Wood, R. Stratocumulus Clouds. *Mon. Weather Rev.* **2012**, *140*, 2373–2423. [CrossRef]
35. Lounesto, P. *Clifford Algebras and Spinors*, 2nd ed.; London Mathematical Society Lecture Note Series; Cambridge University Press: Cambridge, UK, 2001. [CrossRef]
36. Chelton, D.B.; Esbensen, S.K.; Schlax, M.G.; Thum, N.; Freilich, M.H.; Wentz, F.J.; Gentemann, C.L.; McPhaden, M.J.; Schopf, P.S. Observations of Coupling between Surface Wind Stress and Sea Surface Temperature in the Eastern Tropical Pacific. *J. Clim.* **2001**, *14*, 1479–1498. [CrossRef]
37. Hashizume, H.; Xie, S.-P.; Fujiwara, M.; Shiotani, M.; Watanabe, T.; Tanimoto, Y.; Liu, W.T.; Takeuchi, K. Direct Observations of Atmospheric Boundary Layer Response to SST Variations Associated with Tropical Instability Waves over the Eastern Equatorial Pacific. *J. Clim.* **2002**, *15*, 3379–3393. [CrossRef]
38. Pezzi, L.P.; Souza, R.B.; Farias, P.C.; Acevedo, O.; Miller, A.J. Air-Sea Interaction at the Southern Brazilian Continental Shelf: In Situ Observations. *J. Geophys. Res. Ocean.* **2016**, *121*, 6671–6695. [CrossRef]
39. Hennemuth, B.; Lammert, A. Determination of the Atmospheric Boundary Layer Height from Radiosonde and Lidar Backscatter. *Bound. Layer Meteorol.* **2006**, *120*, 181–200. [CrossRef]
40. SeaPAC. QuikSCAT Level 2B Ocean Wind Vectors in 12.5km Slice Composites Version 4.1. Ver. 4.1. PO.DAAC, CA, USA. 2020. Available online: https://podaac.jpl.nasa.gov/dataset/QSCAT_LEVEL_2B_OWV_COMP_12_KUSST_LCRES_4.1 (accessed on 20 August 2021).
41. EUMETSAT/OSI SAF. MetOp-A ASCAT Level 2 25.0 km Ocean Surface Wind Vectors. Ver. Operational/Near-Real-Time. PO.DAAC, CA, USA. 2010. Available online: https://podaac.jpl.nasa.gov/dataset/ASCATA-L2-25km (accessed on 22 January 2022).
42. Copernicus Climate Change Service (C3S) (2017): ERA5: Fifth Generation of ECMWF Atmospheric Reanalyses of the Global Climate. Copernicus Climate Change Service Climate Data Store (CDS). Available online: https://cds.climate.copernicus.eu/cdsapp#!/home (accessed on 3 March 2019).
43. Hersbach, H.; Bell, B.; Berrisford, P.; Hirahara, S.; Horányi, A.; Muñoz-Sabater, J.; Nicolas, J.; Peubey, C.; Radu, R.; Schepers, D.; et al. The ERA5 Global Reanalysis. *Q. J. R. Meteorol. Soc.* **2020**, *146*, 1999–2049. [CrossRef]
44. Cleveland, W.S.; Devlin, S.J. Locally Weighted Regression: An Approach to Regression Analysis by Local Fitting. *J. Am. Stat. Assoc.* **1988**, *83*, 596–610. [CrossRef]

45. Schlax, M.G.; Chelton, D.B. Frequency Domain Diagnostics for Linear Smoothers. *J. Am. Stat. Assoc.* **1992**, *87*, 1070–1081. [CrossRef]
46. de Kloe, J.; Stoffelen, A.; Verhoef, A. Improved Use of Scatterometer Measurements by Using Stress-Equivalent Reference Winds. *IEEE J. Sel. Top. Appl. Earth Obs. Remote Sens.* **2017**, *10*, 2340–2347. [CrossRef]
47. Liu, W.T.; Tang, W. *Equivalent Neutral Wind (NASA Technical Report)*; Jet Propulsion Lab., California Inst. Of Tech.: Pasadena, CA, USA, 1996; No. NASA-CR-203424.
48. Ross, D.M.; Overland, J.E.; Plerson, W.J.; Cardone, V.J.; McPherson, R.J.; Yu, T.-W. Chapter 4 Oceanic Surface Winds. *Adv. Geophys.* **1985**, *27*, 101–140. [CrossRef]
49. Parfitt, R.; Seo, H. A New Framework for Near-Surface Wind Convergence over the Kuroshio Extension and Gulf Stream in Wintertime: The Role of Atmospheric Fronts. *Geophys. Res. Lett.* **2018**, *45*, 9909–9918. [CrossRef]
50. Small, R.J.; de Szoeke, S.P.; Xie, S.; Luke; Seo, H.; Song, Q.Q.; Cornillon, P.; Spall, M.; Minobe, S. Air–Sea Interaction over Ocean Fronts and Eddies. *Dyn. Atmos. Ocean.* **2008**, *45*, 274–319. [CrossRef]
51. Seo, H.; O'Neill, L.W.; Bourassa, M.A.; Czaja, A.; Drushka, K.; Edson, J.B.; Fox-Kemper, B.; Frenger, I.; Gille, S.T.; Kirtman, B.; et al. Ocean Mesoscale and Frontal-Scale Ocean–Atmosphere Interactions and Influence on Large-Scale Climate: A Review. *J. Clim.* **2023**, *36*, 1981–2013. [CrossRef]
52. Small, R.J.; Rousseau, V.; Parfitt, R.L.; Laurindo, L.C.; O'Neill, L.W.; Masunaga, R.; Schneider, N.; Chang, P.S. Near-Surface Wind Convergence over the Gulf Stream—The Role of SST Revisited. *J. Clim.* **2023**, *36*, 5527–5548. [CrossRef]
53. Minobe, S.; Kuwano-Yoshida, A.; Komori, N.; Xie, S.-P.; Small, R.J. Influence of the Gulf Stream on the Troposphere. *Nature* **2008**, *452*, 206–209. [CrossRef]